

EDisCS – the ESO Distant Cluster Survey[★]

Sample Definition and Optical Photometry

S. D. M. White¹, D. I. Clowe², L. Simard³, G. Rudnick¹, G. De Lucia¹, A. Aragón-Salamanca⁴, R. Bender⁵,
P. Best⁶, M. Bremer⁷, S. Charlot¹, J. Dalcanton⁸, M. Dantel⁹, V. Desai⁸, B. Fort¹⁰, C. Halliday¹¹, P. Jablonka¹²,
G. Kauffmann¹, Y. Mellier^{10,9}, B. Milvang-Jensen⁵, R. Pelló¹³, B. Poggianti¹⁴, S. Poirier¹², H. Rottgering¹⁵,
R. Saglia⁵, P. Schneider¹⁶ and D. Zaritsky²

¹ Max-Planck-Institut für Astrophysik, Karl-Schwarzschild-Str. 1, Postfach 1317, D-85741 Garching, Germany

² Steward Observatory, University of Arizona, 933 North Cherry Avenue, Tucson, AZ 85721

³ Herzberg Institute of Astrophysics, National Research Council of Canada, Victoria, BC V9E 2E7, Canada

⁴ School of Physics and Astronomy, University of Nottingham, University Park, Nottingham NG7 2RD, United Kingdom

⁵ Max-Planck Institut für extraterrestrische Physik, Giessenbachstrasse, D-85748 Garching, Germany

⁶ Institute for Astronomy, Royal Observatory Edinburgh, Blackford Hill, Edinburgh EH9 3HJ, UK

⁷ Department of Physics, Bristol University, H. H. Wills Laboratory, Tyndall Avenue, Bristol BS8 1TL

⁸ Astronomy Department, University of Washington, Box 351580, Seattle, WA 98195

⁹ LERMA, UMR8112, Observatoire de Paris, section de Meudon, 5 Place Jules Janssen, F-92195 Meudon Cedex, France

¹⁰ Institut d'Astrophysique de Paris, 98 bis boulevard Arago, 75014 Paris, France

¹¹ Institut für Astrophysik, Friedrich-Hund-Platz 1, 37077 Göttingen, Germany

¹² GEPI, CNRS-UMR8111, Observatoire de Paris, section de Meudon, 5 Place Jules Janssen, F-92195 Meudon Cedex, France

¹³ Laboratoire d'Astrophysique, UMR 5572, Observatoire Midi-Pyrénées, 14 Avenue E. Belin, 31400 Toulouse, France

¹⁴ Osservatorio Astronomico, vicolo dell'Osservatorio 5, 35122 Padova

¹⁵ Sterrewacht Leiden, P.O. Box 9513, 2300 RA, Leiden, The Netherlands

¹⁶ Institut für Astrophysik und Extraterrestrische Forschung, Universität Bonn, Auf dem Hügel 71, 53121 Bonn, Germany

Received ?? ????? 2005; accepted ?? ????? 2005

Abstract We present the ESO Distant Cluster Survey (EDisCS) a survey of 20 fields containing distant galaxy clusters with redshifts ranging from 0.4 to almost 1.0. Candidate clusters were chosen from among the brightest objects identified in the Las Campanas Distant Cluster Survey, half with estimated redshift $z_{\text{est}} \sim 0.5$ and half with $z_{\text{est}} \sim 0.8$. They were confirmed by identifying red sequences in moderately deep two colour data from VLT/FORS2. For confirmed candidates we have assembled deep three-band optical photometry using VLT/FORS2, deep near-infrared photometry in one or two bands using NTT/SOFI, deep optical spectroscopy using VLT/FORS2, wide field imaging in two or three bands using the ESO Wide Field Imager, and HST/ACS mosaic images for 10 of the most distant clusters. This first paper presents our sample and the VLT photometry we have obtained. We present images, colour-magnitude diagrams and richness estimates for our clusters, as well as giving redshifts and positions for the brightest cluster members. Subsequent papers will present our infrared photometry, spectroscopy, HST and wide-field imaging, as well as a wealth of further analysis and science results. Our reduced data become publicly available as these papers are accepted.

Key words. Galaxies: clusters: general – Galaxies: evolution – Galaxies: photometry

1. Introduction

Galaxy clusters were recognised as well defined structures even before the extragalactic nature of the nebulae was established. Shortly after Hubble's monumental discovery they be-

came the systems where the need for unseen “dark” matter was first recognised. Sky surveys using the Schmidt telescopes on Mount Palomar made it possible to compile large catalogues of clusters and these formed the basis of most cluster studies until X-ray detection of the intracluster medium became possible for large cluster samples with the Einstein and ROSAT satellites. In the near future catalogues based on detection through gravitational lensing or through inverse Compton scattering of the microwave background (the Sunyaev-Zel'dovich effect) will

Send offprint requests to: S. White e-mail: swhite@mpa-garching.mpg.de

[★] Based on observations obtained at the ESO Very Large Telescope (VLT) as part of the Large Programme 166.A-0162 (the ESO Distant Cluster Survey).

provide samples selected according to cluster mass and thermal energy content, throwing new light on the relation between galaxies, dark matter, and the intergalactic medium.

Rich galaxy clusters are relatively rare objects and are the most massive quasi-equilibrium systems in the Universe. This has led to two different threads of cluster studies. One focuses on clusters as the high mass tail of cosmic structure formation. Their abundance, clustering and evolution constrain the amplitude, growth rate and statistics of cosmic density fluctuations, and hence both the dark matter content of the Universe and the process responsible for generating all structure within it. The internal structure of clusters and their star and gas content constrain the nature of the dark matter and the cosmic baryon fraction. Recent years have seen a lot of work comparing the cosmological constraints provided by cluster studies with those coming from observations of microwave background fluctuations or of distant type Ia supernovae.

The second thread studies the galaxies themselves. Clusters have always played a major role in galaxy evolution studies. They provide large samples of galaxies at the same redshift in a compact and thus easily observable field. The physical proximity of the galaxies and the dense intracluster medium both lead to strong environmental effects which may cause many of the striking differences between “cluster” and “field” populations. cD galaxies, the most massive stellar systems known, are found almost exclusively in rich clusters, which also house the most energetic radio galaxies at the redshifts where these are most abundant. Only in clusters is the interaction between galaxies and intergalactic gas directly observable. Cluster studies led to the first direct and unambiguous detection of evolution in the “normal” galaxy population, and clusters continue to provide some of the most compelling evidence for the wholesale morphological transformation of galaxies. Finally, clusters provide a critical test of galaxy formation models based on the now standard hierarchical paradigm for the growth of structure.

That galaxies in clusters differ systematically from those in the “field” was originally noticed by Hubble and was explored quantitatively in the 1970’s by Oemler (1974) and Dressler (1980). Nearby rich clusters contain more ellipticals and S0’s and fewer star-forming galaxies than poorer systems, a trend which is particularly marked for concentrated clusters which typically have high X-ray luminosities and central dominant galaxies. This variation can be viewed as a relation between morphology and the local space density of nearby galaxies. Evolution of cluster populations was discovered by Butcher & Oemler (1978); already by $z \sim 0.3$ many (but not all) clusters show a substantial population of blue galaxies not present in significant numbers in nearby systems. Spectroscopy shows some of these objects to be actively forming stars, while others have strong Balmer absorption but no emission lines, indicating the presence of young stars without any current star formation (Dressler & Gunn 1983).

Much recent work has concentrated on the nature of these blue cluster members. The large HST-based study of the “Morphs” group (Dressler et al. 1997, 1999; Poggianti et al. 1999) showed them to have primarily disk-like morphologies and a very wide range of star formation rates. This study also found a population of red spiral galaxies and showed S0 galax-

ies to be less common in $z \sim 0.5$ than in nearby clusters. In contrast, the abundance of ellipticals is similar in nearby and distant clusters and their colours and kinematics suggest purely passive evolution of their stellar populations (Oke 1971; Hamilton 1985; Aragón-Salamanca et al. 1993; Bender et al. 1996; Kodama et al. 1998; van Dokkum & Franx 2001). These properties can also be mimicked, however, by models where ellipticals assemble much later (Kauffmann & Charlot 1998) and data on the mass growth of central cluster galaxies may even favour such a model (Aragón-Salamanca et al. 1998).

A variety of mechanisms have been suggested to explain these trends. The relative lack of disk-dominated and star-forming systems was ascribed to galaxy collisions by Spitzer & Baade (1951) and to interactions with intracluster gas by Gunn & Gott (1972). The first process, the transformation of disk galaxies into spheroidals by tidal shocks, was simulated in some detail by Farouki & Shapiro (1981), and was baptised “galaxy harassment” in the much later numerical study of Moore et al. (1996). The second process, “ram pressure stripping”, was first simulated by Gisler (1976) for ellipticals and has recently been simulated more realistically by Quilis et al. (2000) for spirals. The build-up of massive central galaxies by repeated accretion of other cluster members (“cannibalism”) was proposed by Ostriker & Tremaine (1975) and White (1976a), while Silk (1976) suggested that these objects form from the cooling flows which often surround them. The formation of normal ellipticals through disk-galaxy mergers was proposed by Toomre & Toomre (1972) and has been simulated by many authors beginning with Farouki & Shapiro (1982) and Negroponte & White (1983). Larson et al. (1980) suggested that cluster galaxies may redden because removal of an external gas supply causes them to run out of fuel for star formation (“strangulation”), while Dressler & Gunn (1983) proposed that starbursts truncate star formation in galaxies that are suddenly overpressured by the intracluster medium.

Understanding the roles of these various processes requires a comparison of the observational data with detailed theoretical models for the evolution of clusters and the galaxies within them. Early simulations of cluster formation demonstrated how the regularity of a cluster can be considered a measure of its dynamical age (White 1976b) and two decades later the dynamical build-up of cD galaxies in small clusters could be simulated quite realistically (Dubinski 1998). Simulations which can follow the morphology and stellar content of rich cluster galaxies in the CDM cosmogony have become possible only recently (Kauffmann et al. 1999; Springel et al. 2001). A first detailed comparison with a modern cluster survey was presented by Diaferio et al. (2001). Many of the environmentally driven processes discussed above still remain to be incorporated in such work, however (see Lanzoni et al. (2005) for a first treatment).

Since the early 1980’s many systematic studies of clusters have been based on X-ray selected catalogues. For example, the Einstein Medium Sensitivity Survey (Gioia et al. 1990) provided the base catalogue for the CNOC1 survey of clusters at $z \sim 0.4$ (Carlberg et al. 1996), as well as many of the objects in the Morphs HST survey at similar redshift and the cluster MS1054-03 at $z = 0.83$, until recently the highest redshift cluster studied in any detail (e.g van Dokkum et al. 1999).

Similarly many cluster catalogues have been built from ROSAT data (Böhringer et al. 1998; Rosati et al. 1995; Mullis et al. 2003) and these are providing candidates for ongoing studies of distant clusters, including RXJ0848.9+4452 at $z = 1.26$ which has now taken over from MS1054-03 as the most distant well-studied cluster (Rosati et al. 1999). Substantial studies of optically selected samples have been rarer. Recent wide area optical surveys for distant cluster candidates include those of Postman et al. (1996, 1998), da Costa et al. (1999) and Gonzalez et al. (2001) which cover 6, 16, 17 and 135 square degrees respectively. Very recently, Gladders & Yee (2005) have published candidate lists for the first 10% of their Red Sequence Cluster Survey which covers 100 square degrees. At lower redshifts, the 2dF Galaxy Redshift Survey and the Sloan Digital Sky Survey provide very large samples of uniformly observed galaxy clusters which are ideal for studying the systematic properties of cluster galaxy populations (Gómez et al. 2003; Bahcall et al. 2003; De Propris et al. 2004).

Optical selection of distant clusters has a disadvantage with respect to X-ray selection, in that the incidence of “false positive” candidates caused by line-of-sight superposition of unrelated systems is significantly higher. Thus most of the 9 clusters observed by Oke et al. (1998) are superpositions of a number of peaks, and for about half of them the existence of a real cluster appears dubious. In contrast none of the 16 (lower redshift) CNOC1 clusters has a substantial secondary peak and at most two of the clusters appear dubious. This superposition problem becomes more serious at higher redshift because the contrast of clusters with respect to the foreground becomes lower. It can be reduced but not eliminated by tuning the cluster detection algorithm to be sensitive to the dense inner regions of clusters and to galaxies with the colour of elliptical galaxies at the (unknown) cluster redshift.

An optimised filter was used to detect cluster candidates in the Las Campanas Distant Cluster Survey (LCDCS) on which our own survey is based (Gonzalez et al. 2001). We chose the LCDCS as the basis for our ESO Distant Cluster Survey (EDisCS) because it was, at the beginning of our project, by far the largest uniformly covered area over which one could detect clusters (either at optical or X-ray wavelengths) to redshifts of 0.9 or so. Its nominal volume at $z > 0.7$ is larger than the entire local volume within $z = 0.1$. We wished to select samples of rich clusters at $z \sim 0.5$ and $z \sim 0.8$ which were large and diverse enough to be statistically representative and for which we could obtain sufficient data to compare the galaxy populations in detail with those in nearby clusters. Our principal goal is to understand quantitatively the evolution of the cluster galaxy population over the last half of the Hubble time. Optical selection is an advantage here, since similarly selected nearby cluster samples can be constructed and analysed using the Sloan Digital Sky Survey. Our data provide an interesting comparison to other recent distant cluster surveys which are primarily X-ray selected.

The data we have obtained in the EDisCS programme are of uniform and very high quality, and they allow us not only to discuss the structure, stellar populations and kinematics of cluster galaxies out to $z \sim 0.8$, but also to carry out weak and strong lensing programmes, AGN searches, field studies and a

variety of other programmes which help characterise our clusters and global galaxy evolution since $z \sim 0.8$. In Sect. 2 we set out the EDisCS programme in more detail and we go through our sample selection and confirmation procedures. Our optical photometry, obtained using FORS2 at the VLT, is presented in Sect. 3. We take a first look at our clusters in Sect. 4, showing images, colour-magnitude diagrams and morphology plots and giving positions and redshifts for all of them, as well as discussing each cluster individually. We give a brief summary in Sect. 5. Our infrared photometry, optical spectroscopy, HST and wide-field imaging are discussed in later papers of this series, as are a wide variety of scientific results.

2. The EDisCS Programme

The parent catalogue of our ESO Distant Cluster Survey (EDisCS) is the Las Campanas Distant Cluster Survey of Gonzalez et al. (2001). The LCDCS region is a strip 90 degrees long and 1.5 degrees wide centred at $RA = 12.5$ hours and $\delta = -12^\circ$. This strip was observed with a purpose-built drift-scan camera attached to the Las Campanas Observatory 1m telescope. A very wide filter (~ 4500 to $\sim 7700\text{\AA}$) maximised the signal-to-noise of distant clusters against the sky. Each point appears in at least two drift scans, and the observing technique allows the elimination of cosmic rays and bad CCD columns, as well as excellent flat-fielding and sky subtraction. Resolved objects are detected and replaced with locally drawn random sky pixels. Saturated stars and large galaxies are also masked. Any remaining structure in the image is due to spatial variation in the background light. Large-scale structure is removed by subtracting a heavily smoothed version of the image itself (filter radius $70''$). Clusters are then detected by convolving with an exponential kernel matched to the expected core size of galaxy clusters at $z \sim 0.8$ (an exponential scale radius of $10''$). The limiting surface brightness for a 5σ detection of a cluster is roughly 28 mag/sq.arcsec in I (for $R - I = 1^1$) and just over 1000 candidate clusters with estimated redshifts in the range 0.3 to 1.0 are detected at this level; about 15 per cent have estimated redshifts beyond 0.8. Redshifts can be estimated almost to $z = 0.9$ from the apparent magnitude of the brightest cluster member. At higher redshifts even the BCG is not individually detected, even though the integrated cluster brightness may still be easily measurable.

The EDisCS programme is a detailed spectroscopic and photometric survey of the galaxy populations of 10 among the highest surface brightness clusters in the LCDCS in each of the ranges $0.45 < z_{\text{est}} < 0.55$ and $0.75 < z_{\text{est}} < 0.85$. In the following we will refer to these as the “mid- z ” and “hi- z ” samples respectively. We aimed for 10 clusters at each redshift both because of the substantial cluster-to-cluster variation in galaxy populations seen at $z \sim 0.4$ (cf the CNOC and MORPHs work) and because of our wish to obtain statistics for relatively rare cluster populations (cDs, radio galaxies, other AGN...). Two redshift bins seemed a minimum to see evolution directly in our own data. Samples of 15 to 20 bright candidate clusters were selected from the LCDCS lists in each red-

¹ Throughout this paper we use Vega magnitudes.

shift range. Each field was checked carefully to ensure that the detection appeared reliable and free from observational artifacts. These candidate lists were then followed up in order of their estimated brightness in a structured observing programme for which seven phases are now complete.

Phase I: Confirmation Photometry: We observed our two candidate lists in LCDCS luminosity order using FORS2 at the VLT. We first obtained 20 minute exposures of 30 fields at I and either at V (mid- z sample) or at R (hi- z sample). We used these to confirm the presence of an apparent cluster with a brightest member of approximately the magnitude expected. This was necessary since in most cases very few galaxies were detected individually in the original LCDCS drift scans. We also checked for the presence of a possible red sequence of early-type galaxies at the expected location in the colour-magnitude diagram. Candidates failing either of these tests were rejected and replaced with the next brightest candidate. In practice it was necessary to observe 13 “mid- z ” LCDCS fields and 17 “hi- z ” fields in order to obtain 10 photometrically confirmed clusters in each estimated redshift range. The statistics of these observations and their implications for the completeness of the LCDCS are analysed in Gonzalez et al. (2002).

Phase II: Deep Optical Photometry: We then obtained deep FORS2 photometry at B, V and I for a final set of 10 photometrically confirmed mid- z clusters and at V, R and I for a final set of 10 photometrically confirmed hi- z clusters. Our total integration times were typically 45 minutes at the lower redshift and 2 hours at the higher redshift. Image quality in all exposures was excellent. The FORS2 field is $6'.8 \times 6'.8$ with a pixel size of $0''.20$. After dithering, the field of view with the maximum depth of exposure was approximately $6.5' \times 6.5'$. These are the data presented in more detail in this first EDisCS paper. (See Sect. 3.1 and Table 1 for further details.) A weak-shear analysis of gravitational lensing by our clusters, based on these same data, is presented in Clowe & et al. (2005).

Phase III: Deep Near-Infrared Photometry: For all but two of this same set of 20 cluster fields, we carried out deep near-infrared imaging using SOFI at the NTT, obtaining at least 150 minutes of exposure at K_s for each mid- z cluster and at least 300 minutes at J and 360 minutes at K_s for each hi- z cluster. The SOFI field is $5'.5 \times 5'.5$ with a pixel size of $0''.29$. The field of view of our SOFI images, taking account of the dithering and overlapping of exposures, is $6.0' \times 4.2'$ for our mid- z clusters and $5.4' \times 4.2'$ for our hi- z clusters; see Aragón-Salamanca et al. (2005, in prep.) for details. Poor weather prevented observation of the last two of our mid- z fields. These data allow us to characterise better the spectral energy distributions, stellar masses and sizes of cluster members, and to obtain reliable photometric redshifts for eliminating many foreground and background galaxies. They will be presented in detail in Aragón-Salamanca et al. (2005, in prep.). Our photometric redshifts will be presented in Pelló et al. (2005, in prep.).

Phase IV: Confirmation Spectroscopy: We used the multi-object slit-mask capability of FORS2 to obtain spectra with 30 minutes (mid- z) or 60 minutes (hi- z) exposure for the candidate brightest cluster member and for up to 30 other candidate cluster members in each photometrically confirmed cluster field. Redshift histograms were then constructed to confirm the pres-

ence of a redshift spike in the range expected. One field was rejected at this stage because its redshift histogram suggested that the detected object was a superposition of a number of groups spread out in redshift, with no dominant cluster.

Phase V: Deep Spectroscopy: For 18 of the 19 remaining spectroscopically confirmed clusters we next obtained deep spectroscopy using 3 to 5 separate slit masks on FORS2 and exposure times of typically 60–120 minutes (mid- z) or 240 minutes (hi- z). This resulted in samples of between 10 and 70 members in each cluster with an average of about 30. For the 19th cluster we were able only to get one further 20 minute integration with the existing mask. The spectra are of sufficient quality to obtain both stellar population and kinematic information (velocity dispersions for E/S0 galaxies, rotation velocities from [OII] $\lambda 3727$ for big disk galaxies). Our spectroscopic observation procedures are presented in detail together with data for our first 5 clusters in Halliday et al. (2004). The data for the remaining 15 clusters will be presented in Milvang-Jensen et al. (2005, in preparation).

Phase VI: Wide-field Imaging: In order to obtain information about the large-scale structure in which our clusters are embedded, we have used the Wide-Field Imager at the ESO/MPG 2.2m telescope to obtain ~ 120 minute exposures of each of our fields at R and ~ 60 minute exposures in V and I. The larger-scale environments of our clusters will be studied using these data in Clowe et al. (2005b, in prep.).

Phase VII: HST/ACS Imaging: For 10 of our highest redshift clusters we have obtained mosaic images with one orbit exposure in the outer regions and 5 orbit coverage at cluster centre using the Advanced Camera for Surveys on board the Hubble Space Telescope. These data are particularly useful, in combination with our deep VLT photometry, for studying the morphology of our cluster galaxies. The data will be presented and the HST morphologies analysed in Desai et al. (2005, in prep.).

At the time of writing, data taking is finished for all phases with the final observations obtained in spring 2004. Data reduction is completed for phases I, II, III, IV, VI and VII and is almost completed for phase V. Thus while we do not, at this stage, have final results or interpretation for many aspects of the survey, we do have enough information from all phases to give a clear view of the size and quality of the final dataset. In this paper we present our optical photometry in detail and give basic information about the cluster sample, reserving detailed discussion of our other observations and the presentation of our main results for future papers in this series.

3. Optical photometry with FORS2

3.1. The observations

Our deep optical imaging programme was carried out using FORS2 in direct imaging mode on the VLT. Our goal was to obtain 120 minutes of high image quality integration in V, R, and I for every cluster in the final hi- z sample and 45 minutes of integration in B, V, and I for every cluster in the mid- z sample. These are the standard FORS2 filters. B, V and I are close approximations to the Bessell (1990) photometric system

while the R filter is a special filter for FORS2.² The imaging was performed in two phases - a contiguous 5 night period in visitor mode between March 19 and March 24 2001, and 50 hours in service mode taken between April and July 2001, and in January and February 2002. Two of the nights during the March 2001 observations were photometric and all 20 clusters had 10 minutes of integration, taken in two 5 minute exposures, in all three passbands during these nights. These short exposures were used to define our photometric zero-points, and all of our other images were then scaled to these zero-points by comparing the flux in bright but unsaturated stars. A list of the final exposure times, FWHM seeing measurements and 5σ limiting magnitudes (for a $1''$ radius aperture) is given in Table 1.

3.2. Production of calibrated images

The images were reduced with the following steps. First a master bias frame was scaled row-by-row to a linear 1-D fit to the over-scan strip of each image and subtracted. A 3σ clipped, medianed night-sky flat was then created for each night in each band (or over contiguous nights if only a single field was obtained on a given night in the service mode observations) and was used to flat-field the images. A bad pixel map was created from lists of pixels either with exceptionally bright bias levels or with very low values in the normalised flat-field. Next, the sky was fit and subtracted using two different methods, resulting in two sets of sky-subtracted data. For both methods, the IMCAT³ *findpeaks* peak finder was inverted to detect local minima in images smoothed with a $1''$ Gaussian to create a catalogue of local sky measurements. The first method fit a bi-cubic polynomial to these sky measurements, and subtracted the polynomial from the unsmoothed image. The second method used a $6''.5$ Gaussian interpolation and smoothing method to create a sky-image which was subtracted from the unsmoothed image. This higher resolution sky-image corrected small-scale variations in the sky level, but also subtracted the extended wings of saturated stars and of the larger, foreground galaxies, as well as any intergalactic light which might be present in the clusters.

An additional sky-subtraction step was deemed necessary as the I images had a residual slope, after flat-fielding, along the east-west axis which correlated with the total sky level. Comparison of the photometry of objects in the same field among images with differing sky levels (and therefore differing slopes) did not reveal a similar slope in the photometry. We therefore subtracted a linear fit to this sky variation in order to remove it prior to combining images. This minimises differences in sky level across the field. The images with high and low resolution sky subtraction were used to produce catalogues for different purposes as noted below.

The IMCAT *findpeaks* peakfinder was used on both sets of sky-subtracted data to detect bright but unsaturated stars. The positions of these stars were then compared to the USNO catalogue and to the positions in the other exposures of the same

field to derive both a correction for camera distortion and the linear offset between the fields. Each image was then distortion corrected and aligned using a triangular method which preserves surface brightness to map the images onto a common reference frame for each field. This resulted in an alignment of the individual images to each other with a stellar *rms* position error of ~ 0.05 pixels ($\sim 0''.01$), and an *rms* position offset between the images and the USNO catalogue which varied from $0''.4$ to $0''.6$ among the 20 fields. A final image was then created using a sky-noise weighted mean with a clipping algorithm which removed a pixel from the mean calculation if its value was more than 3σ from the median *and* differed from the median by more than 50 per cent of the difference between the median and the sky level. The second condition prevents clipping the centres of stars in images with slightly different *psf*'s than the median.

The images created with the polynomial-fit sky-subtraction are used for our photometric analysis and are the images on which the rest of this paper is based. The images created with the Gaussian-interpolated sky-subtraction are used in our weak lensing analysis of the clusters, which is presented in Clowe et al. (2005a). A third set of images, created with the polynomial fit sky-subtraction but without any distortion correction during the mapping, were used to determine slit positions for our spectroscopy. No colour-term correction was applied to put these images on the standard BVRI system because these corrections are very small for the FORS2 filter/CCD combination, smaller than the errors on our photometric zeropoints. (From the dispersion in the values we obtain for our standards, we estimate these zeropoint errors to be 0.018, 0.013, 0.013 and 0.016 magnitudes in B, V, R and I, respectively.)

3.3. Catalogue construction

In order to produce optical/IR photometric catalogues which are as uniform as possible, we decided to match the seeing FWHM on all our optical and IR images to $0''.8$. (This was the typical seeing in our IR images; see Aragón-Salamanca et al. (2005, in prep.).) This matching was done wherever needed *and* possible. The few images with FWHM significantly larger than $0''.8$ were left untouched. The following steps were used: (1) I-band images were degraded to $0''.8$ when necessary using a Gaussian convolution kernel (IRAF/GAUSS), and (2) images in the other filters were similarly degraded until their “plumes” of stars in a size versus magnitude plot overlapped with the I-band plumes. The plumes were very well-defined, and this made the matches quite straightforward.

Photometry on these seeing-matched images was carried out using SExtractor version 2.2.2 (Bertin & Arnouts 1996). SExtractor was run in “two-image” mode using the I-band images as detection reference images. Note that in cases where the cluster I-band images needed to be degraded to $0''.8$, the *original* I-band images were used as the detection reference images. Thus our catalogues are all based on detection in I-band at the original observed resolution, which was often better than $0''.8$, but our magnitudes (including those in I-band) are measured whenever possible from images with FWHM of $0''.8$. Our pho-

² The FORS2 filter curves are given at <http://www.eso.org/instruments/fors/inst/Filters/curves.html>

³ See <http://www.ifa.hawaii.edu/~kaiser/imcat>.

Table 1. FORS2 optical imaging: filters, exposure times, final seeing and 5σ limiting magnitudes

mid-z clusters	I			V			B		
	t_{exp} [min]	FWHM ["]	m_{lim}	t_{exp} [min]	FWHM ["]	m_{lim}	t_{exp} [min]	FWHM ["]	m_{lim}
1018.8–1211	60	0.77	24.9	60	0.80	26.1	45	0.80	26.5
1059.2–1253	60	0.75	24.7	60	0.85	26.2	45	0.80	26.4
1119.3–1129	45	0.58	24.8	45	0.52	26.2	40	0.58	26.5
1202.7–1224	45	0.64	24.9	45	0.75	26.0	45	0.70	26.4
1232.5–1250	45	0.52	24.8	50	0.63	26.2	45	0.56	26.4
1238.5–1144	45	0.54	24.8	45	0.63	26.1	45	0.61	26.6
1301.7–1139	45	0.56	24.9	45	0.64	26.2	45	0.58	26.4
1353.0–1137	45	0.58	25.0	45	0.68	26.1	45	0.60	26.2
1411.1–1148	45	0.48	25.0	45	0.60	26.2	45	0.59	26.4
1420.3–1236	45	0.74	24.9	45	0.80	26.1	45	0.62	26.4
hi-z clusters	I			R			V		
	t_{exp} [min]	FWHM ["]	m_{lim}	t_{exp} [min]	FWHM ["]	m_{lim}	t_{exp} [min]	FWHM ["]	m_{lim}
1037.9–1243	120	0.56	25.1	130	0.54	26.1	120	0.55	26.6
1040.7–1155	115	0.62	25.1	120	0.72	26.0	120	0.62	26.5
1054.4–1146	115	0.72	25.1	150	0.78	26.1	120	0.67	26.6
1054.7–1245	115	0.50	25.4	110	0.77	26.1	120	0.79	26.5
1103.7–1245	115	0.64	25.3	120	0.75	26.1	130	0.83	26.4
1122.9–1136	115	0.65	25.2	115	0.70	25.9	120	0.71	26.3
1138.2–1133	125	0.60	25.2	110	0.68	26.0	120	0.58	26.5
1216.8–1201	115	0.60	25.3	110	0.72	26.0	130	0.68	26.6
1227.9–1138	145	0.74	25.1	130	0.83	26.0	155	0.73	26.4
1354.2–1230	115	0.66	25.2	120	0.70	26.0	125	0.70	26.4

Note: m_{lim} are 5σ limiting magnitudes in a $r = 1''.0$ aperture on our images convolved to $0''.8$ seeing as estimated using the empty aperture simulations described in the text.

photometric catalogues contain five types of I-band magnitude – magnitudes in circular apertures of radius 1, 2 and $3''$, isophotal magnitudes and SExtractor Kron (i.e. MAG–AUTO) magnitudes. All isophotal magnitudes for each galaxy are measured within the *same* pixel set, defined to correspond to the I-band isophote which is 1.5σ above the sky background. Similarly our Kron magnitudes in all bands are measured within the aperture which SExtractor defines for each galaxy based on its I-band image. We estimate an approximate “total” I-magnitude for each galaxy by adding to the Kron magnitude the correction appropriate for a point source measured within an aperture equal to the galaxy’s Kron aperture. This correction is obtained from an empirical “curve of growth” constructed from the images of bright, unsaturated and isolated stars on each convolved I-band image. It will underestimate the correction needed obtain realistic *total* magnitudes, particularly for large galaxies. At $I_{\text{tot}} \sim 25$ the median correction from Kron to “total” magnitude ranges from 0.06 to 0.10 magnitudes for our clusters. At these limits the median Kron magnitudes are themselves up to 0.5 magnitudes brighter than the median isophotal magnitudes and up to 0.2 magnitudes brighter than the median magnitude within a $1''$ aperture.

Throughout this paper we correct our magnitudes and colours for Galactic extinction according to the maps of Schlegel et al. (1998) and a standard Milky Way reddening curve. We used the galactic extinction curve to derive the expected extinction at the central wavelength of each of our fil-

ters. The reddening value at each cluster’s position is listed in Table 2. We made no attempt to estimate or correct for differential reddening across our fields. Our catalogues, released with this paper, list data, uncorrected for Galactic extinction, for all objects with “total” I-band magnitudes, defined as above using the convolved images, brighter than $I = 24.0$ in the mid-z fields and brighter than $I = 24.5$ in the deeper hi-z fields (cf Figure 1).

Our catalogues are available in electronic form at the CDS. The tables provide 64 columns containing: the galaxy ID; the object RA and Dec (J2000); five types of magnitude (1,2,3 arc-sec radius aperture magnitudes as well as isophotal, SExtractor MAG AUTO magnitudes) and their corresponding errors for the B, V, I (mid-z) and V, R, I (hi-z) bands; a point source aperture correction; the “total” I magnitude (MAG AUTO+correction) and its corresponding error; the SExtractor object flag in B, V, I (mid-z) and V, R, I (hi-z) bands; the SExtractor Stellerity index in the same bands; the SExtractor half-light radius in these bands; the SExtractor object ellipticity; the SExtractor object position angle; the SExtractor object semi-major axis; the SExtractor object semi-minor axis; the SExtractor object Kron radius; and the SExtractor object isophotal area.

3.4. Catalogue completeness

Understanding the completeness of our photometric catalogues is important for many of our applications, but is far from simple. Objects appear in the catalogues if SExtractor detects them

in our original I-band images, even though the various magnitudes we quote are measured from the seeing-matched images. Our completeness is high for galaxies whose I-band magnitude within a $1''$ radius aperture (after convolution to our fiducial seeing) is above the 5σ limiting magnitude given in Table 1. Such objects are normally lost only if they become confused with other images. On the other hand, objects with significantly brighter *total* magnitudes may be lost if they have large sizes. In Fig. 1 we show differential number counts in the I-band for all of our fields. Star images have been removed from these counts based on colour information and on the size-magnitude relation for unresolved objects. The counts turn over sharply at the same point in all fields in each set and at “total” I magnitudes comparable to the 5σ limits of Table 1. This is a clear sign of incompleteness. The scatter between the counts in different fields is larger than the counting errors, demonstrating the well-known result that large-scale structure very substantially affects counting statistics in fields of the size studied here (46 sq. arcmin.). Comparison with deeper I-band counts from the two Hubble Deep Fields (Metcalf et al. 1998) and from the FORS Deep Field (Heidt et al. 2003) as well as with somewhat shallower counts over a much larger area from the COMBO-17 survey (Wolf et al. 2003) shows very good agreement. Our completeness clearly remains high to magnitudes significantly fainter than $I = 24$.

3.5. Photometric errors

Accurate photometric errors for galaxy colours are extremely important for reliable photometric redshift determinations. Realistic errors for galaxy magnitudes are also important for many aspects of the analysis we will carry out in later papers.

Our aperture and isophotal magnitudes are not intended as estimates of the total light of our galaxies, but rather of the light in their images within the chosen aperture after convolution to our fiducial seeing with FWHM $0''.8$. The uncertainty in such quantities is typically much less than in total magnitudes for which the major source of scatter is a seeing-, model- and object-dependent “aperture correction”. This is why galaxy colours are much more reliably estimated by differencing aperture or isophotal magnitudes than by differencing total magnitudes. (Note that the isophote radius must be defined in one band, the I-band in our case, and then used consistently for all filters. Note also that the “total” magnitudes discussed above and plotted in Fig. 1 are not intended as accurate measures of total light, but rather as robust lower limits which should approximate the true total light for small and faint galaxies.) The errors in such colours should not depend on galaxy structure or on seeing, but only on photon noise. For our convolved images the photon noise in neighbouring pixels is correlated and is dominated by sky counts for the great majority of objects. We therefore estimate this noise as the *rms* scatter in the photon count over many apertures of each relevant size placed at random in areas of each field where SExtractor detects no object (for details see Labbé et al. 2003). Errors in colours can then be estimated as the sum in quadrature of the errors in the two relevant aperture magnitudes. This method ignores the possible

contribution from systematic effects which correlate between different bands observed with the same instrument, as can arise, for example, from background sources which fall beneath our detection threshold.

Although errors in our fixed aperture magnitudes (e.g. our standard 1, 2 and $3''$ apertures) are correctly estimated in this way, there is an additional source of error in our isophotal, Kron and “total” magnitudes (though not in colours derived from them) which comes from the uncertainty in estimating the size of the isophote (or the Kron radius). Such errors can only be estimated by careful Monte Carlo experiments in which artificial “galaxies” are inserted into real images and their properties measured just as for the real galaxies. They depend on the exact magnitude definition and on the details of the photometric software. We will report on such Monte Carlo experiments for our EDisCS data in future papers where we require accurate error estimates for specific applications.

We illustrate our error estimates in Fig. 2, which gives scatter plots of the error in our I-band “total” magnitudes and in our $V - I$ colours as a function of “total” magnitude for typical mid- z and hi- z fields. Note that in this and subsequent figures we shorten slightly the names of the clusters to save space. The colours for this plot are computed using either the $1''$ or the isophotal apertures for objects depending on whether they are or are not flagged as being crowded by SExtractor. As just discussed, these are the errors due to sky noise in the relevant apertures as estimated from the convolved images. They should thus be accurate for the colour but somewhat too small for the “total” magnitude because of the failure to include the uncertainty in the measured Kron radius itself. These errors are small all the way down to our estimated completeness limit (see § 3.4). This can be understood by recalling that SExtractor requires at least 4 adjacent pixels to be at least 1.5 sigma above the estimated sky background in the filtered SExtractor detection image. Particularly for extended objects this is a stringent requirement and causes objects to drop out of the sample when the errors in their AUTO magnitudes are small.

4. The EDisCS Cluster Sample

In this section we give basic information to characterise our sample of clusters as a whole, together with a short description of each cluster. Fig. 3 presents false colour images of a square field $3'$ on a side centred on the galaxy which we identify as the brightest member of each cluster (BCG; see the discussion of individual clusters below for detail on how the BCG’s were selected). These were constructed by combining the three available optical images using a stretch which maximises the variation of image colour with galaxy spectral energy distribution and so makes it easy to recognise galaxies with similar colours, in particular red sequence galaxies near the redshift of each cluster (see Lupton et al. 2004). The colours and luminosities of the BCG candidates themselves are plotted against redshift in Fig. 4 and are compared with a Bruzual & Charlot (2003) model for evolution from a single, solar metallicity burst of star formation at redshift 3. The luminosity of the burst is normalised to give $M_V = -22.4$ at $z = 0$; this is the absolute magnitude of NGC4889, the brightest galaxy in the Coma Cluster.

The colours and the magnitudes of all our BCG candidates are consistent with this passive evolution model.

In Fig. 5 we show I versus $V - I$ colour magnitude diagrams within a 1.0 Mpc radius circle centred on the BCG of each cluster.⁴ These were made using I -band “total” magnitudes and colours within $1''$ radius apertures. We reject all galaxies for which our photometric redshift programmes give a low probability of cluster membership. We derive photometric redshifts from our optical + near-IR photometry using two independent codes (Bolzonella et al. 2000; Rudnick et al. 2001, 2003) both calibrated using our own spectroscopy; see Pelló et al. (2005, in prep.) for details. Briefly we accept galaxies as potential cluster members if the integrated photometric redshift probability to be within $z \pm 0.1$ of the cluster redshift is greater than a specific threshold for *both* of the photometric redshift codes. These probability thresholds were calibrated using our spectroscopy and range from 0.1-0.35 depending on the filter set available for each particular field. No further statistical correction for residual field contamination has been made because the field of our infrared photometry does not extend much beyond the region used to make the plots. We will come back to the issue of residual contamination in later work. Objects with sizes consistent with those of unresolved point sources and spectral energy distributions consistent with those of faint Galactic stars are rejected. The population of galaxies along the red sequence of some of these clusters is analysed in De Lucia et al. (2004).

The galaxy we identify as the candidate BCG is shown in each colour-magnitude diagram by a large cross. The almost horizontal solid line gives the position of the red sequence predicted by fitting the above Bruzual & Charlot model to the Coma cluster assuming that the slope reflects a dependence of metallicity on stellar mass (i.e. fixing $z_{\text{burst}} = 3$ for all masses). Parallel dashed lines at ± 0.2 magnitudes in colour delineate the band we use to estimate a characteristic richness for each cluster. We define this as the count of galaxies in this band brighter than the apparent magnitude which translates to $M_V = -18.2$ when evolved passively to $z = 0$ with our standard model. This apparent magnitude is shown as a vertical solid line in each plot. It was chosen so that all objects counted are above the 5σ detection limit in all of our clusters with the exception of the most distant object (cl1103.7–1245) which was identified late (see below). Finally, the steep slanting dashed lines in each plot correspond to our 5 , 3 and 1σ detection limits in the V -band. Note that our richness measure is not corrected for residual contamination. We estimate how large this may be as follows. Our photo- z rejection eliminates between 10 and 30 galaxies (median 18) from the bands of the colour-magnitude plots used for our richness count. We have looked at the count distribution for colour-magnitude bands in random patches of one field of the Canada-France Deep Field Survey (McCracken et al. 2001) whose C-M position and area are matched to each of our clusters in turn. The median count in these field patches ranges from 25 to 33 for the 20 clusters, but the count in different fields matched to the same cluster ranges from below 10 to over 50,

with a typical interquartile range of a factor of 1.6. Thus our richness count is probably biased high by about 10 galaxies, but the large expected fluctuation in background count makes any case-by-case correction for residual contamination extremely uncertain.

In Fig. 6 we give isopleths of the density of galaxies brighter than $I = 25$ in 4.8×4.8 fields centred on our BCG candidates after rejection of probable non-members and stars as above. Our cuts reject 80 to 90 per cent of all objects to this magnitude limit, while rejecting fewer than 10 per cent of our spectroscopically confirmed cluster members. This region is the largest square field for which we have both IR and optical data for most of our clusters. These contours were made by adaptive kernel smoothing in a scheme very similar to that outlined by Pisani (1993, 1996). The position of our BCG candidate in each field is marked by a cross. An artifact should be noted in these plots; the densities always drop close to the field boundary because we have not attempted to correct for boundary effects. Note also that for two clusters we do not have IR data and in these fields our photometric redshift techniques are less efficient at rejecting non-members (cf Table 2).

Numerical data for each cluster are given in Table 2 which lists the cluster name, the position, its original ID in the LCDCS, the reddening value adopted for each field, I -band “total” apparent magnitude, $V - I$ colour (both corrected for Galactic extinction) and redshift of the BCG, as well as the measure of cluster richness we discussed above. We reiterate that this is effectively a count of “red sequence” galaxies above a fixed stellar mass limit, so that its relation to the total richness of a cluster depends on the relative proportions of red and blue galaxies. As may be seen from Fig. 5, our sample shows large variations in this ratio. Some clusters appear to show a strong red sequence with rather few blue galaxies (e.g. cl1232.5–1250, cl1138.2–1133) while others show many blue galaxies but relatively few passively evolving systems (e.g. cl1238.5–1144, cl1040.7–1155, cl1227.9–1138). This is an interesting result which may in part reflect differences in foreground/background contamination. We will come back to it again in later papers.

Our clusters were originally taken from the LCDCS lists. In many fields the identification of the cluster and the associated BCG is unambiguous, based on the available spectroscopy, the brightness, colour, and spatial distributions of galaxies in the images, their photometric redshifts and our weak lensing maps. Nevertheless, there were some fields where it was not possible to conclusively identify the BCG. We will not discuss the spectroscopic redshifts, lensing maps, or photometric redshifts in detail here, since these will be presented elsewhere (Halliday et al. 2004; Clowe et al. 2005a; Milvang-Jensen et al. 2005, Clowe et al. 2005b, Pelló et al. 2005, all in prep.). We do, however, give a description of each cluster based on all currently available information. This includes the basis for our current identification of the BCG and redshift of the cluster, together with our current assessment of the structure and richness of the cluster based on the images and colour-magnitude diagrams of Figs. 3 and 5. The spectroscopic data for 5 of our clusters (cl1232.5–1250, cl1040.7–1155, cl1054.4–1146, cl1054.7–1245, and cl1216.8–1201) were

⁴ Throughout this paper we assume a flat cosmology with $\Omega_m = 0.3$ and $H_0 = 70 \text{ km s}^{-1} \text{ Mpc}^{-1}$ whenever we quote quantities in physical rather than observed units.

Table 2. Cluster Data

Cluster	BCG Coordinates ^a	LCDCS ID	E(B-V)	I ^b	V-I ^c	z	Richness ^d	Filters
1018.8–1211	10:18:46.8 -12:11:53	0057	0.077	17.96	2.16	0.47	46	BVIK _s
1059.2–1253	10:59:07.1 -12:53:15	0188	0.033	17.84	2.14	0.46 ^e	51	BVIK _s
1119.3–1129	11:19:16.7 -11:30:29	0252	0.066	19.24	2.18	0.55	28	BVI
1202.7–1224	12:02:43.4 -12:24:30	0430	0.058	18.40	1.99	0.42	39	BVIK _s
1232.5–1250	12:32:30.5 -12:50:36	0541	0.060	18.20	2.36	0.54	105	BVIJK _s
1238.5–1144	12:38:33.0 -11:44:30	0567	0.044	18.37	2.19	0.46	32	BVI
1301.7–1139	13:01:40.1 -11:39:23	0634	0.049	18.27	2.21	0.48	48	BVIK _s
1353.0–1137	13:53:01.7 -11:37:28	0849	0.063	18.64	2.44	0.59	28	BVIK _s
1411.1–1148	14:11:04.6 -11:48:29	0925	0.065	18.25	2.24	0.52	45	BVIK _s
1420.3–1236	14:20:20.0 -12:36:30	0952	0.082	18.53	2.24	0.50	37	BVIK _s
1037.9–1243	10:37:51.2 -12:43:27	0110	0.043	18.54	2.29	0.58 ^e	22	VRIJK _s
1040.7–1155	10:40:40.4 -11:56:04	0130	0.051	19.87	2.49	0.70	23	VRIJK _s
1054.4–1146	10:54:24.5 -11:46:20	0172	0.037	19.49	2.56	0.70	53	VRIJK _s
1054.7–1245	10:54:43.6 -12:45:52	0173	0.038	19.61	2.68	0.75	33	VRIJK _s
1103.7–1245	11:03:43.4 -12:45:34	0198	0.048	20.68	2.73	0.96	15	VRIJK _s
1103.7–1245a	11:03:34.9 -12:46:46		0.048	19.54	2.46	0.63		VRIJK _s
1103.7–1245b	11:03:36.5 -12:44:22		0.048	19.46	2.57	0.70		VRIJK _s
1122.9–1136	11:22:51.6 -11:36:32	0275	0.040	19.50	2.23	0.64	15	VRIJK _s
1138.2–1133	11:38:10.3 -11:33:38	0340	0.027	18.63	2.09	0.48	49	VRIJK _s
1216.8–1201	12:16:45.1 -12:01:18	0504	0.045	19.46	2.63	0.80	74	VRIJK _s
1227.9–1138	12:27:58.9 -11:35:13	0531	0.047	19.33	2.41	0.63	28	VRIJK _s
1354.2–1230	13:54:09.7 -12:31:01	0853	0.079	19.47	2.53	0.76	22	VRIJK _s

^a Coordinates (J2000) of our BCG candidate^b BCG “total” magnitude from SExtractor AUTO-MAG + a minimal point source correction (always < 0.04mag for these galaxies)^c BCG colour measured within a $r = 1''$ circular aperture^d Number of red-sequence galaxies within 1 Mpc of the BCG (after photo-z rejection of non-members) and brighter than the apparent I magnitude which evolves passively to $M_V = -18.2$ at $z = 0$ ^e Redshift of the cluster – no spectroscopy for BCG

presented in (Halliday et al. 2004). The data for the remaining 15 clusters will be presented in Milvang-Jensen et al. (2005, in preparation).

Finally we note that one field (cl1103.7–1245) has three clusters listed in Table 2. As we discuss below, when we reduced our deep spectroscopy for this field we discovered a distant cluster at the LCDCS position but at a substantially higher redshift ($z = 0.96$) than that inferred from our confirmation spectroscopy and so built into our spectroscopic targeting strategy. At the lower redshift two substantial groupings showed up in the field but centred away from the LCDCS position. Our BCG candidates for all three structures are plotted in Fig. 4, and colour-magnitude diagrams and isopleths are shown for the lower redshift range in the last panels of Fig. 5 and Fig.6, respectively, after photo-z rejection of foreground and background galaxies.

Mid-z clusters

cl1018.8–1211: Redshifts are available for 69 galaxies in this field. In the corresponding spectroscopic redshift histogram there is a clear peak of more than 30 spectroscopically confirmed members at $z = 0.47$. There is also a peak in the photometric redshift probability distribution at $z \approx 0.47$. The isopleths of Fig. 6 show a clear concentration of galaxies around the cluster centre with a second concentration about $3'$ to the southwest. There is a 3.0σ detection in the weak lensing map centred on the concentration of red galaxies in the image.

The colour-magnitude diagram suggests a well defined red sequence with a significant blue population. The brightest galaxy at the LCDCS position is at the centre of the galaxy distribution and has a redshift in the spectroscopic peak. We identify this galaxy, EDCSNJ1018467–1211527, as the BCG.

cl1059.2–1253: Redshifts are available for 86 galaxies in this field. In the spectroscopic redshift histogram there is a clear peak of 40 objects at $z = 0.46$. There is also a peak in the photometric redshift probability distribution at $z \approx 0.45$. The isopleths show a very strong peak at the LCDCS position. There is a 5.2σ detection in the weak lensing map centred on this concentration of red galaxies. The colour-magnitude diagram demonstrates that this is a rich cluster with a well-defined red sequence but also with many bluer galaxies. The brightest galaxy at the LCDCS position is near the centre of the galaxy distribution, it has a photometric redshift equal to 0.42, but does not have a measured spectroscopic redshift. We identify this galaxy, EDCSNJ1059071–1253153, as the BCG.

cl1119.3–1129: Redshifts are available for 57 galaxies in this field. The redshift histogram has 22 objects at $z = 0.55$, and there is a peak in the photometric redshift probability distribution at $z \approx 0.55$. The isopleths show no clear concentration of galaxies in the field and there is no weak lensing detection. The colour-magnitude diagram shows a relatively strong red sequence at the expected colour but bluer galaxies appear absent (perhaps because the absence of K-band data affects our

photometric redshift probabilities in this field). The identification of the BCG is uncertain; there are multiple bright galaxies in the vicinity of the LCDCS detection which could be the BCG. For now, we treat the object EDCSNJ1119168–1130290 as the BCG since we have a spectrum. It is fainter than expected for a BCG, however (see Table 2 and Fig. 4) and there are candidates with similar colours and brighter magnitudes in the field, but with no spectroscopy.

cl1202.7–1224: Redshifts are available for 62 galaxies in this field. The redshift histogram has a dominant peak with more than 20 objects at $z = 0.42$. There is also a peak in the photometric redshift probability distribution at $z \approx 0.42$. The isopleths in this field show a clear concentration near the expected position. There is a 1.5σ detection in the weak lensing map centred on the concentration of red galaxies. The colour-magnitude diagram shows a clear red sequence at the expected colour with a few bluer galaxies. The brightest galaxy at LCDCS position is quite close to the centre of the galaxy distribution and has a redshift in the spectroscopic peak. We identify this galaxy, EDCSNJ1202433–1224301, as the BCG.

cl1232.5–1250: Redshifts are available for 100 galaxies in this field. This is one of our richest clusters with a peak of 54 objects in the spectroscopic redshift histogram at $z = 0.54$. There is also a peak in the photometric redshift probability distribution at $z \approx 0.54$. The isopleths show a strong and highly elongated concentration and there is a 7.6σ detection in the weak lensing map centred on this concentration. The colour-magnitude diagram shows a very strong red sequence but also a substantial population of bluer galaxies. The brightest galaxy near the LCDCS position is close to the centre of the galaxy distribution. We identify this galaxy, EDCSNJ1232303–1250364, as the BCG.

cl1238.5–1144: This cluster has the poorest spectroscopic coverage in our sample, with only two short exposure masks obtained. Redshifts are available for only 10 galaxies in the field. Because of the obvious weakness of this cluster it was assigned low priority for long-exposure spectroscopy, and it is the only one of our 19 retained clusters for which we eventually obtained *no* longer exposure masks. In the first mask there are at least 4 galaxies at $z = 0.46$. There is a broad peak in the photometric probability distribution at $z \sim 0.45$. The broadness of the peak is probably due to the lack of NIR data in this field. There is a concentration in the isopleths at the expected position but it is very weak. Furthermore there is no weak lensing detection for this field. The colour-magnitude diagram shows a relatively strong red sequence at the expected colour. The brightest galaxy at the LCDCS position is close to the peak of the isopleths and has a redshift in the spectroscopic peak. We identify this galaxy, EDCSNJ1238330–1144307, as the BCG.

cl1301.7–1139: Redshifts are available for 85 galaxies in this field. The redshift histogram of this field has 37 objects at $z = 0.48$ and 16 objects at $z = 0.39$. The coordinate of the LCDCS source matches that of the brightest galaxy in the 0.48 peak. The photometric redshift probability distribution has a peak at $z \approx 0.48$, but nothing obvious at 0.40. The isopleths in the field show two clear concentrations separated by about $2'$. The southeastern peak is the $z = 0.48$ cluster targeted from the LCDCS, the northwestern peak is likely the

0.4 cluster. There is a spatially extended weak lensing detection at 3.4σ that overlaps with the galaxy concentrations in the two peaks. The red sequence in the colour-magnitude diagram is strong and appears concentrated at the colour expected for the higher redshift. There is also a substantial population of blue galaxies. The 0.48 structure was the one selected by the LCDCS and we choose the brightest galaxy in this concentration, EDCSNJ1301402–1139229, as the BCG.

cl1353.0–1137: Redshifts are available for 65 objects in this field. The redshift histogram has at least 27 objects at $z = 0.58$. There is also a peak in the photometric redshift probability histogram at $z \approx 0.58$. The isopleths are peaked at the expected position, but less strongly than in many of our other clusters. A peak in the lensing map also coincides with the obvious galaxy concentration on the image at the location of the LCDCS source. The colour-magnitude diagram shows a well-defined but relatively poor red-sequence at the expected colour. There is a substantial population of bluer galaxies. The brightest galaxy at the position of the LCDCS source is located at the centre of the galaxy distribution and has $z = 0.59$. We identify this galaxy, EDCSNJ1353017–1137285, as the BCG.

cl1411.1–1148: Redshifts are available for 73 galaxies in this field. There are 23 objects at $z = 0.52$. There is also a peak in the photometric redshift probability histogram at $z \approx 0.52$. The isopleths show a strong and relatively symmetric concentration at the expected position. There is a peak in the lensing map coincident with this concentration which is also at the LCDCS location. The colour magnitude diagram shows a red sequence which appears slightly redder than expected. There are fewer blue galaxies here than in many of our clusters. The brightest galaxy at the LCDCS position has a redshift in the spectroscopic peak. We identify this galaxy, EDCSNJ1411047–1148287, as the BCG.

cl1420.3–1236: Redshifts are available for 70 galaxies in this field. In the redshift histogram there are 26 objects at $z = 0.49$. There is also a peak in the photometric redshift probability histogram at $z \approx 0.50$. The isopleths have a clear and symmetric peak at the expected position, but although there is a 2.7σ peak in the lensing map, it is not perfectly coincident with the galaxy concentration (which does coincide with the LCDCS source). The colour-magnitude diagram for this field shows a weak red sequence at the expected colour in addition to the population of bluer galaxies. The brightest galaxy at the LCDCS position is near the peak of the isopleths and has a redshift in the spectroscopic peak. We identify this galaxy, EDCSNJ1420201–1236297, as the BCG.

Hi- z clusters

cl1037.9–1243: Redshifts are available for 117 galaxies in this field. The spectroscopic redshift histogram for cl1037.9–1243 is complex with two dominant peaks at $z = 0.42$ (43 members) and 0.58 (19 members). The relative strengths of the peaks may be biased by our targeting brighter galaxies for our initial spectroscopy. There is an obvious cigar-shaped cluster in this field at the position of the LCDCS source with a concentration of red galaxies of similar colour. While the objects in the 0.43 spike are spread over the whole field, the objects in the 0.58 spike are concentrated around the LCDCS source position. There is a peak in the photometric redshift

probability distribution at $z \approx 0.58$, but our photo- z 's do not perform well at $z \lesssim 0.5$ for the hi- z filter set (cf. Table 2). Objects with photo- z 's around 0.58 are concentrated at the position of the cigar while the objects with z_{phot} consistent with 0.42 are concentrated towards the west side of the image. The isopleths for the field are quite complex with no obvious dominant peak. All the principal structures seen in the isopleths are also detected in the weak lensing map. In the colour-magnitude diagram there is no clear red sequence at $z = 0.58$ but a reasonably well populated one at $z \sim 0.42$ (compare with *cl1202.7–1224*). Although there is obviously a rich cluster at 0.42, the object selected by the LCDCS nevertheless appears to be the cluster at $z = 0.58$. Our original choice for the BCG was resolved into two objects by our ACS image of this cluster. The brighter of these may still turn out to be the BCG, but there are also other bright objects in the cluster core. We provisionally select one of these, EDCSNJ1037514–1243266, as the BCG of the $z = 0.58$ structure. For this galaxy, we do not have spectroscopic information.

cl1040.7–1155: Redshifts are available for 130 galaxies in this field. In the spectroscopic redshift histogram there is a peak of 30 objects at $z = 0.70$. There is also a peak in the photometric redshift probability distribution at $z \approx 0.70$. The isopleths show a single dominant concentration at the LCDCS position but no significant mass concentration is detected in the weak lensing map. The colour magnitude relation shows a remarkably weak red sequence but a substantial population of bluer galaxies. The brightest galaxy near the LCDCS position is centred on the peak of the isopleths and has a redshift in the spectroscopic peak. We identify this galaxy, EDCSNJ1040403–1156042, as the BCG.

cl1054.4–1146: Redshifts are available for 109 galaxies in this field. In the spectroscopic redshift histogram there are 49 cluster members at $z = 0.70$. There is a peak in the photometric redshift probability distribution at $z \approx 0.70$. The dominant peak in the isopleths is at the LCDCS position which also coincides with a concentration in the weak lensing mass map. The colour-magnitude diagram shows a well developed red sequence at the expected colour but also a population of bluer galaxies including some bright objects. The brightest galaxy near the LCDCS position is at the peak of the isopleths and has a redshift in the spectroscopic peak. We identify this galaxy, EDCSNJ1054244–1146194, as the BCG, although there are other possible candidates of similar colour and slightly brighter magnitude.

cl1054.7–1245: Redshifts are available for 104 galaxies in this field. In the spectroscopic redshift histogram there are 36 objects at $z = 0.75$, as well as a group of 10 galaxies at $z = 0.73$ which is about 7σ away from the main cluster where σ is the cluster velocity dispersion (Halliday et al. 2004). There is a peak in the photometric redshift probability distribution at $z \approx 0.75$. The galaxy isopleths show a strong peak at the LCDCS position and there is also a strong concentration in the weak lensing mass at this position. This cluster has a well developed red sequence which appears somewhat redder than the expected colour, together with a substantial population of bluer galaxies, again including a number of bright galaxies. As can be seen in Fig. 3, this cluster has one or

two strongly lensed arcs directly north of our BCG candidate. This is EDCSNJ1054435–1245519, the brightest galaxy at the LCDCS position. It is centred on the isopleth peak and has a redshift in the spectroscopic peak.

cl1103.7–1245: Redshifts are available for 100 galaxies in this field. Our initial spectroscopy showed a number of galaxies in the redshift range 0.6 to 0.7, so we used our photometric redshifts to reject objects far from this redshift when selecting targets for deep spectroscopy. The final spectroscopic redshift histogram indeed shows peaks at $z = 0.70$ (11 members) and 0.63 (14 members). There is also, however, a peak containing nine objects at $z = 0.96$ despite our targetting bias against such high redshifts. There are peaks in the photometric redshift probability distribution at $z \sim 0.65$, at $z \sim 0.70$ and also at $z \sim 0.95$. The brightest galaxies at $z = 0.63$ and $z = 0.70$ are located quite far away from the LCDCS position, but the brightest galaxy in the 0.96 peak coincides with the LCDCS position and with a bright field galaxy at $z = 0.66$. We have made two sets of colour-magnitude and isopleth plots, one rejecting galaxies with photo- z 's incompatible with $z = 0.96$, and the other rejecting galaxies incompatible with $z = 0.66$ (in order to include the structures at redshifts 0.63 and 0.70). We show the plots for the $z = 0.96$ case labelled *cl1103–1245* in figures 5 and 6, where the C-M diagram is for a circle radius 1.0 Mpc surrounding the BCG, as for the other clusters. The plots for the $z = 0.66$ case are also shown, and are labelled *cl1103–1245a/b*. The C-M diagram here is for the full region for which we have five band photometry. The isopleths at $z = 0.96$ show a single peak close to the LCDCS position. At $z = 0.66$ the structure is more complex with several peaks. The weak lensing maps indicate a 3σ detection near the LCDCS source, but also a detection near the brightest galaxy at $z = 0.63$, while we do not have any detection close to the brightest galaxy at $z = 0.7$. There is also a grouping of red galaxies around the brightest $z = 0.63$ galaxy – no such overdensity of red objects is apparent around the brightest galaxy at $z = 0.70$. The colour-magnitude diagrams show reasonably well-defined red sequences at the expected colours. We consider the $z = 0.96$ cluster at the LCDCS position as the selected cluster and choose its brightest galaxy, EDCSNJ1103434–1245341 at $z = 0.9576$, as BCG. Both the $z = 0.63$ and the $z = 0.70$ concentrations also contain bright galaxies with the visual and photometric properties of BCG's. These are EDCSNJ1103349–1246462 at $z = 0.6257$ and EDCSNJ1103365–1244223 at $z = 0.7031$; we give their properties in Fig. 4 and Table 2 where they are denoted *cl1103.7–1245a* and *cl1103.7–1245b*, respectively.

cl1122.9–1136: From the 2002 (short exposure) mask there was no evidence of a concentration of galaxies at any specific redshift in this field. In addition, our photo- z 's show no clear peak and our weak lensing map does not have a significant maximum. The isopleths do show a convincing peak at the LCDCS position which coincides with a galaxy with $z = 0.64$ with approximately the colour and magnitude expected for a BCG. This is presumably what the LCDCS detected. On the other hand, our final colour-magnitude plot shows no convincing red sequence at the expected colour. After some discussion we decided to drop this field from our spectroscopic programme, thus no mask with long exposure

was observed. Our initial candidate for BCG was the galaxy EDCSNJ1122517–1136325.

cl1138.2–1133: Redshifts are available for 106 galaxies in this field. Although this field was originally selected as one of our high redshift clusters, the dominant peak in spectroscopic redshift histogram (48 galaxies) is at $z = 0.48$ and coincides spatially with the LCDCS source and the concentration of red galaxies in the image. (It turns out that the LCDCS overestimated the redshift of this cluster because the cluster centre and the true BCG lay behind the mask.) The isopleths show a single well defined peak within an elongated filament-like structure. Although there are also 5 galaxies at $z = 0.62$, these are spread over the field. Our photometric redshifts are not robust at $z \lesssim 0.5$ for the hi- z filter set (cf. Table 2) and we do not find a peak corresponding to the spectroscopic peak. There is a weak lensing concentration at the location of the LCDCS source. The colour-magnitude diagram shows a tight red sequence at bright magnitudes and at the colour expected for $z = 0.48$. There are surprisingly few blue galaxies or red sequence galaxies at fainter magnitudes, but this might be related to the problem of estimating reliable photometric redshifts with this z and filter set. The brightest galaxy at the LCDCS position is centred on the isopleth peak and has a redshift in the spectroscopic peak. We identify this galaxy, EDCSNJ1138102–1133379, as the BCG.

cl1216.8–1201: This is one of our richest and highest redshift clusters. Redshifts are available for 120 galaxies in the field. In the spectroscopic redshift histogram there are 66 objects at $z = 0.79$. There is a peak in the photometric redshift distribution at the redshift of the cluster and a 6.3σ weak lensing detection which overlaps with the galaxy concentration. There is also a strongly lensed arc in this cluster. The isopleths show a strong peak at the expected position but also several additional peaks which may be cluster substructure. The colour-magnitude diagram shows a very well developed red sequence and also a well defined and well populated sequence of (presumably) star-forming galaxies about 1.5 mag bluer. The brightest galaxy at the LCDCS position is centred on the isopleth peak and has a redshift in the spectroscopic peak. We identify this galaxy, EDCSNJ1216453–1201176, as the BCG.

cl1227.9–1138: Redshifts are available for 113 galaxies in this field which has a complicated structure. There is a dominant peak of 22 objects at $z = 0.63$. There are, however, at least 2 other spikes at $z = 0.49$ and 0.83 , and a broad concentration near 0.58 . The galaxies at $z = 0.63$ coincide with the LCDCS detection, but so do those in the $z = 0.49$ peak. There is also a peak in the photometric redshift probability distribution at $z \approx 0.63$, but none at $z = 0.49$ (perhaps because of the poor performance of our photo- z estimates for this filter set at $z \lesssim 0.5$). The strongest peak in the isopleths is indeed close to the LCDCS position but there are 5 or 6 additional peaks in the field. There is no clear weak lensing detection associated with any of these. The colour-magnitude diagram does show a possible red sequence at $z = 0.63$ but the brightest red galaxies appear to be associated with a red sequence at $z = 0.49$. There are many blue galaxies in the colour-magnitude range expected for objects at either of these redshifts. We believe that the $z = 0.63$ spike is the cluster picked by the LCDCS.

The galaxy EDCSNJ1227539–1138173 is the brightest object with a spectroscopic redshift at $z = 0.63$ near the centre of the red galaxy concentration and the LCDCS position. Its magnitude, however, is significantly fainter than expected for a BCG and the galaxy EDCSNJ1227589–1135135 about 2 arcmin to the north is about 1.2 magnitudes brighter and has redshift $z = 0.6375$. We provisionally choose this latter object as the BCG, although in this case we still centre the false colour image, the C-M diagram, the isopleths, and calculate the richness for a 1.0 Mpc circle surrounding EDCSNJ1227539–1138173 and the LCDCS position.

cl1354.2–1230: Redshifts are available for 116 galaxies in this field. In the spectroscopic redshift histograms there are 20 objects at $z = 0.76$, and smaller peaks at $z = 0.52$ and 0.59 . The composite nature of the spectroscopic redshift histogram may be a result of the wider than normal photo- z interval used to select galaxies for spectroscopy. This wider interval was used because the initial 2002 spectroscopy showed the secondary spike at $z = 0.6$ and we were unsure which was the dominant cluster. There are also peaks in the photometric redshift probability distribution at $z \approx 0.6$ and 0.7 . The isopleths in this field show a strong peak very close to the LCDCS position but there are clearly a number of subsidiary peaks in the field. There is a 3.9σ lensing detection centred on the dominant peak which is a concentration of red galaxies. These show up in our colour-magnitude diagram as a relatively poor red sequence at the expected colour. The fainter red sequence is remarkably empty, but there are plenty of blue cluster members at the expected colours and magnitudes. The brightest galaxy near the main isopleth peak has a spectroscopic redshift of $z = 0.76$, and we identify this galaxy, EDCSNJ1354098–1231015, as the BCG of a cluster at this redshift.

5. Conclusion

The sample of clusters we present here has been uniformly selected and uniformly observed. Moreover, the quality of the data delivered by the ESO telescopes is uniformly high, thanks to the superb instrumentation, the good conditions at Paranal, and the possibility of obtaining data in service mode. The estimated redshifts provided by the LCDCS scatter by 0.06 – 0.08 *rms* about the true values and are systematically high by about 0.1 at high redshift. As a result we have ended up with a set of clusters distributed relatively smoothly in redshift between 0.42 and 0.96 , rather than two samples concentrated at 0.5 and 0.8 as originally planned. Because the LCDCS detection algorithm was only sensitive to cluster light in the inner one to two hundred kpc, our set of clusters has a broad range of richness and internal structure on larger scales. As in all optically selected samples, our cluster set contains a few superpositions of significant objects at differing redshifts. The effect is smaller, however, than in earlier surveys based on detecting light enhancements over larger areas (e.g. Oke et al. (1998); da Costa et al. (1999)). The velocity dispersions of our systems, as estimated both from our lensing maps and from our spectroscopy, span the range from a few hundred to over one thousand km s^{-1} . Our richest clusters are similar to those detected by X-ray surveys for distant objects, but we also have less regular and lower rich-

ness systems. The diversity of the population is evident in the isopleth maps and the colour-magnitude diagrams presented above. Not only do the internal structure and the total galaxy number of the clusters vary dramatically, but so also do the relative numbers of red and blue and of faint and bright galaxies within them. This diversity makes our sample ideal for studying the environmental dependence of galaxy evolution, particularly when our data at half the present age of the Universe are compared with the low-redshift baseline now available with very large statistics and uniform photometric and spectroscopic data from the Sloan Digital Sky Survey. Such studies of the evolution of the galaxy population form the basis for later papers in this series.

Acknowledgements. We have benefitted from the generosity of the ESO/OPC. We thank Henry McCracken for providing us with catalogues from the CFDFs. G. D. L. and S. C. thank the Alexander von Humboldt Foundation, the Federal Ministry of Education and Research, and the Programme for Investment in the Future (ZIP) of the German Government for financial support. G. R. thanks Special Research Area No 375 of the German Research Foundation for financial support.

References

- Aragón-Salamanca, A., Baugh, C. M., & Kauffmann, G. 1998, *MNRAS*, 297, 427
- Aragón-Salamanca, A., Ellis, R. S., Couch, W. J., & Carter, D. 1993, *MNRAS*, 262, 764
- Bahcall, N. A., McKay, T. A., Annis, J., et al. 2003, *ApJS*, 148, 243
- Bender, R., Ziegler, B., & Bruzual, G. 1996, *ApJ*, 463, L51
- Bertin, E. & Arnouts, S. 1996, *A&AS*, 117, 393
- Bessell, M. S. 1990, *PASP*, 102, 1181
- Böhringer, H., Guzzo, L., Collins, C. A., et al. 1998, *The Messenger*, 94, 21
- Bolzonella, M., Miralles, J.-M., & Pelló, R. 2000, *A&A*, 363, 476
- Bruzual, G. & Charlot, S. 2003, *MNRAS*, 344, 1000
- Butcher, H. & Oemler, A. 1978, *ApJ*, 219, 18
- Carlberg, R. G., Yee, H. K. C., Ellingson, E., et al. 1996, *ApJ*, 462, 32
- Clowe, D. & et al. 2005, *A&A*, in press
- da Costa, L., Scodreggio, M., Olsen, L. F., et al. 1999, *A&A*, 343, L29
- De Lucia, G., Poggianti, B. M., Aragón-Salamanca, A., et al. 2004, *ApJ*, 610, L77
- De Propris, R., Colless, M., Peacock, J. A., et al. 2004, *MNRAS*, 351, 125
- Diaferio, A., Kauffmann, G., Balogh, M. L., et al. 2001, *MNRAS*, 323, 999
- Dressler, A. 1980, *ApJ*, 236, 351
- Dressler, A. & Gunn, J. E. 1983, *ApJ*, 270, 7
- Dressler, A., Oemler, A. J., Couch, W. J., et al. 1997, *ApJ*, 490, 577
- Dressler, A., Smail, I., Poggianti, B. M., et al. 1999, *ApJS*, 122, 51
- Dubinski, J. 1998, *ApJ*, 502, 141
- Farouki, R. & Shapiro, S. L. 1981, *ApJ*, 243, 32
- Farouki, R. T. & Shapiro, S. L. 1982, *ApJ*, 259, 103
- Gioia, I. M., Maccaro, T., Schild, R. E., et al. 1990, *ApJS*, 72, 567
- Gisler, G. R. 1976, *A&A*, 51, 137
- Gladders, M. D. & Yee, H. K. C. 2005, *ApJS*, 157, 1
- Gómez, P. L., Nichol, R. C., Miller, C. J., et al. 2003, *ApJ*, 584, 210
- Gonzalez, A. H., Zaritsky, D., Dalcanton, J. J., & Nelson, A. 2001, *ApJS*, 137, 117
- Gonzalez, A. H., Zaritsky, D., Simard, L., Clowe, D., & White, S. D. M. 2002, *ApJ*, 579, 577
- Gunn, J. E. & Gott, J. R. I. 1972, *ApJ*, 176, 1
- Halliday, C., Milvang-Jensen, B., Poirier, S., et al. 2004, *A&A*, 427, 397
- Hamilton, D. 1985, *ApJ*, 297, 371
- Heidt, J., Appenzeller, I., Gabasch, A., et al. 2003, *A&A*, 398, 49
- Kauffmann, G. & Charlot, S. 1998, *MNRAS*, 294, 705
- Kauffmann, G., Colberg, J. M., Diaferio, A., & White, S. D. M. 1999, *MNRAS*, 303, 188
- Kodama, T., Arimoto, N., Barger, A. J., & Aragón-Salamanca, A. 1998, *A&A*, 334, 99
- Labbé, I., Franx, M., Rudnick, G., et al. 2003, *AJ*, 125, 1107
- Lanzoni, B., Guiderdoni, B., Mamon, G. A., Devriendt, J., & Hatton, S. 2005, preprint, astro-ph/0502490
- Larson, R. B., Tinsley, B. M., & Caldwell, C. N. 1980, *ApJ*, 237, 692
- Lupton, R., Blanton, M. R., Fekete, G., et al. 2004, *PASP*, 116, 133
- McCracken, H. J., Le Fèvre, O., Brodwin, M., et al. 2001, *A&A*, 376, 756
- Metcalf, N., Ratcliffe, A., Shanks, T., & Fong, R. 1998, *MNRAS*, 294, 147
- Moore, B., Katz, N., Lake, G., Dressler, A., & Oemler, A. 1996, *Nature*, 379, 613
- Mullis, C. R., McNamara, B. R., Quintana, H., et al. 2003, *ApJ*, 594, 154
- Negroponte, J. & White, S. D. M. 1983, *MNRAS*, 205, 1009
- Oemler, A. J. 1974, *ApJ*, 194, 1
- Oke, J. B. 1971, *ApJ*, 170, 193
- Oke, J. B., Postman, M., & Lubin, L. M. 1998, *AJ*, 116, 549
- Ostriker, J. P. & Tremaine, S. D. 1975, *ApJ*, 202, L113
- Pisani, A. 1993, *MNRAS*, 265, 706
- Pisani, A. 1996, *MNRAS*, 278, 697
- Poggianti, B. M., Smail, I., Dressler, A., et al. 1999, *ApJ*, 518, 576
- Postman, M., Lauer, T. R., Szapudi, I., & Oegerle, W. 1998, *ApJ*, 506, 33
- Postman, M., Lubin, L. M., Gunn, J. E., et al. 1996, *AJ*, 111, 615
- Quilis, V., Moore, B., & Bower, R. 2000, *Science*, 288, 1617
- Rosati, P., della Ceca, R., Burg, R., Norman, C., & Giacconi, R. 1995, *ApJ*, 445, L11
- Rosati, P., Stanford, S. A., Eisenhardt, P. R., et al. 1999, *AJ*, 118, 76
- Rudnick, G., Franx, M., Rix, H., et al. 2001, *AJ*, 122, 2205
- Rudnick, G., Rix, H., Franx, M., et al. 2003, *ApJ*, 599, 847
- Schlegel, D. J., Finkbeiner, D. P., & Davis, M. 1998, *ApJ*, 500,

525

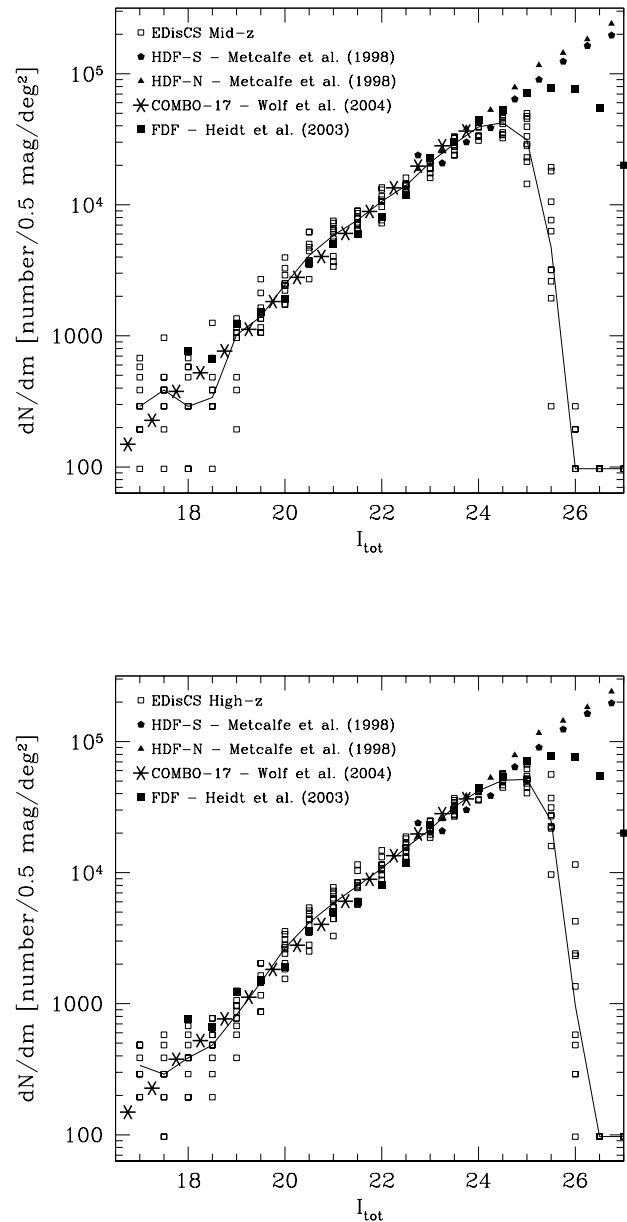
Silk, J. 1976, *ApJ*, 208, 646Spitzer, L. J. & Baade, W. 1951, *ApJ*, 113, 413Springel, V., White, S. D. M., Tormen, G., & Kauffmann, G. 2001, *MNRAS*, 328, 726Toomre, A. & Toomre, J. 1972, *ApJ*, 178, 623van Dokkum, P. G. & Franx, M. 2001, *ApJ*, 553, 90van Dokkum, P. G., Franx, M., Fabricant, D., Kelson, D. D., & Illingworth, G. D. 1999, *ApJ*, 520, L95White, S. D. M. 1976a, *MNRAS*, 174, 19White, S. D. M. 1976b, *MNRAS*, 177, 717Wolf, C., Meisenheimer, K., Rix, H.-W., et al. 2003, *A&A*, 401, 73

Figure 1. Differential number counts in the I-band for all of our fields and separately for the mid-z and hi-z samples. Counts are given as the number per square degree per 0.5 magnitude bin. For comparison we also show deeper counts for the two Hubble Deep Fields (Metcalfe et al. 2001) and for the FORS Deep Field (Heidt et al. 2003) as well as shallower counts over a wider area from the COMBO-17 survey (private communication, see Wolf et al. (2003)). The thin solid line connects median count values for the ten EDisCS fields in each plot.

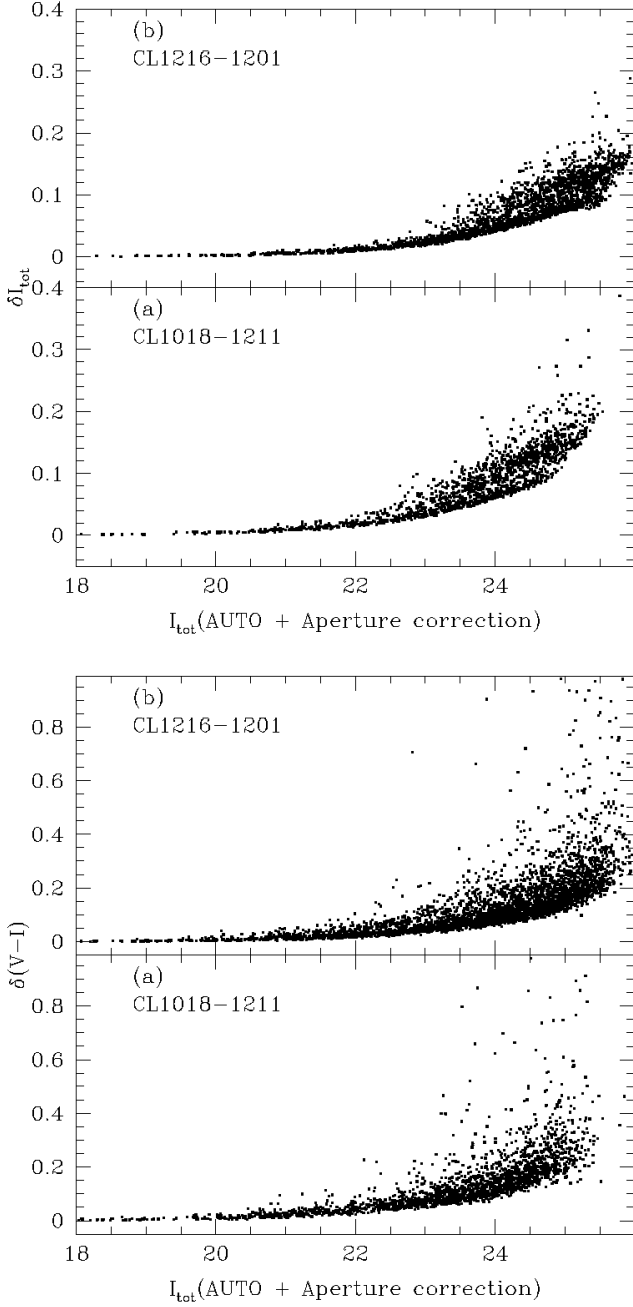


Figure 2. Errors in our “total” I-band magnitudes and in our $V - I$ colours are shown as a function of “total” I-band magnitude for typical fields from our mid- z and hi- z samples. These values were derived from Monte Carlo evaluation of the background count variance in apertures of the size used to measure the actual galaxy magnitudes (see text for details).

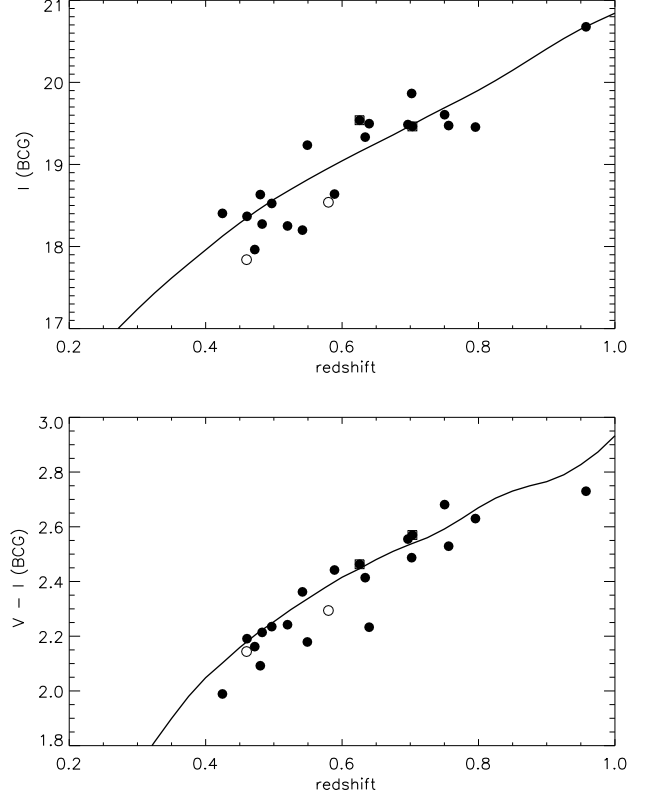


Figure 4. “Total” I-band apparent magnitudes and $V - I$ colours of our BCG candidates are plotted against redshift. The lines in each plot are taken from a Bruzual & Charlot (2003) model which assumes passive evolution after a single, solar metallicity burst of star formation at $z = 3$. The luminosity of the model is normalized so that at $z = 0$ it reproduces the V-band absolute magnitude of NGC4889, the brightest galaxy in the Coma cluster. In both plots, open symbols correspond to the clusters cl1059.2–1253 and cl1037.9–1243, for which we do not have a spectroscopic redshift for the object identified as BCG. In these cases, we use the cluster redshift. The filled squares correspond to the BCG candidates in the two additional structures away from the LCDSCS detection in field 1103.7–1245.

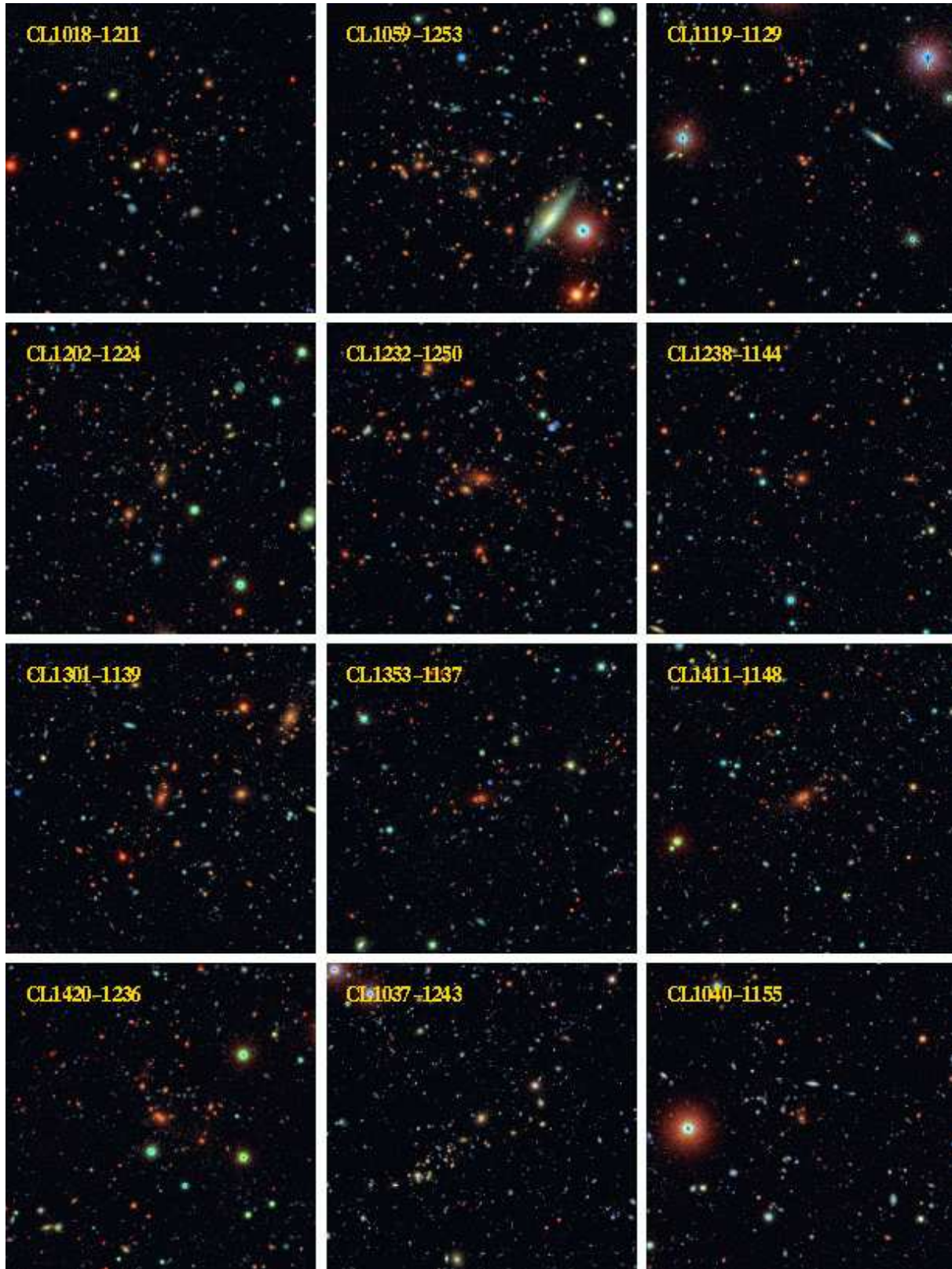


Figure 3.

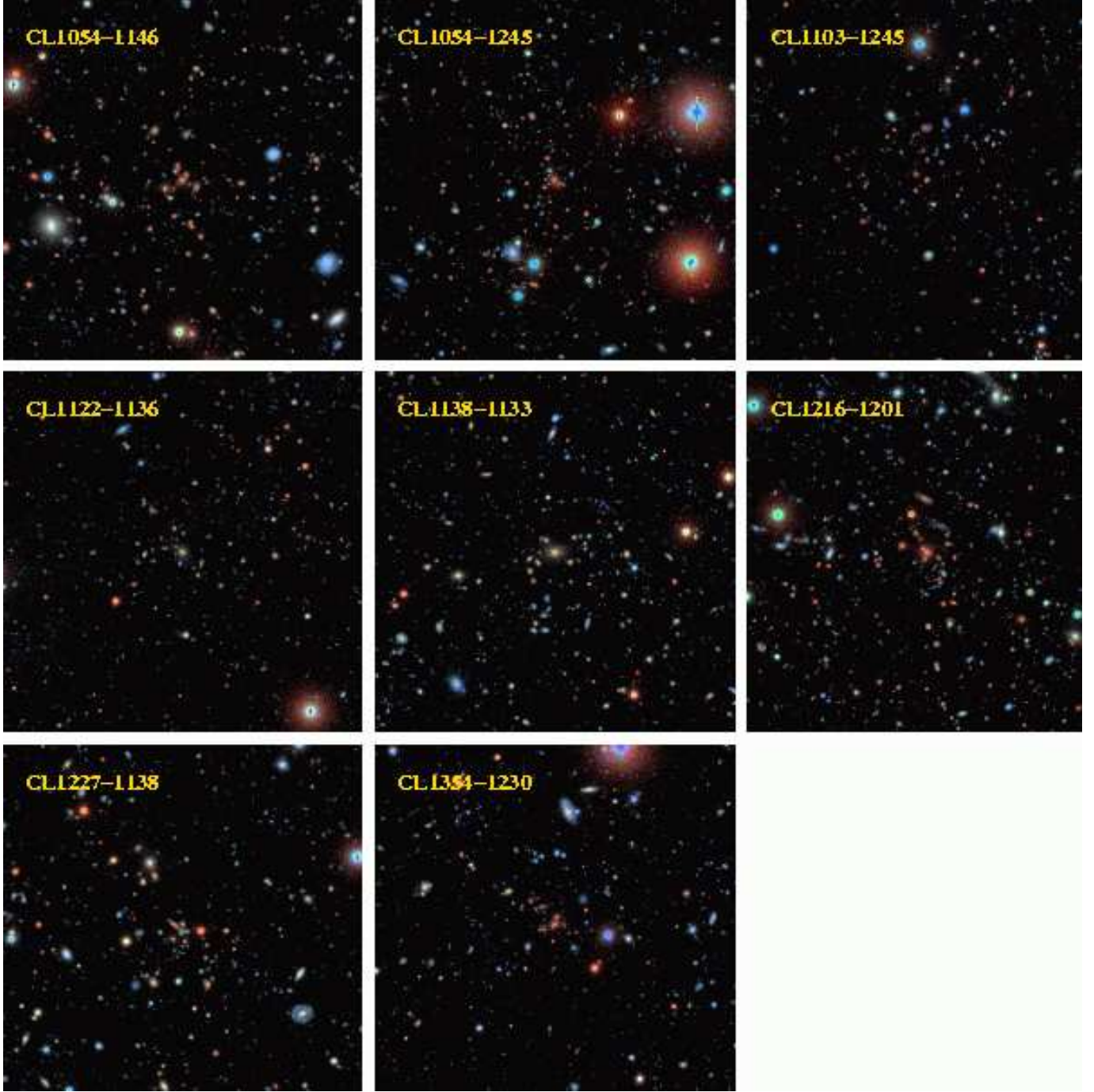


Figure 3. –continued. False colour images of the central regions of each of our EDisCS fields. Each image is $3' \times 3'$ and is centred on our BCG candidate (except for cl1227.9–1138, see text). The images are made by combining the seeing matched images in our three optical bands with a colour stretch which maximizes the variation of image colour with galaxy spectral energy distribution. These colour scales are the same within the mid- z and within the hi- z sample but differ between the two. In each image north is at the top and east is to the left. Images of our mid- z sample in RA order are followed by images of our hi- z sample also in RA order.

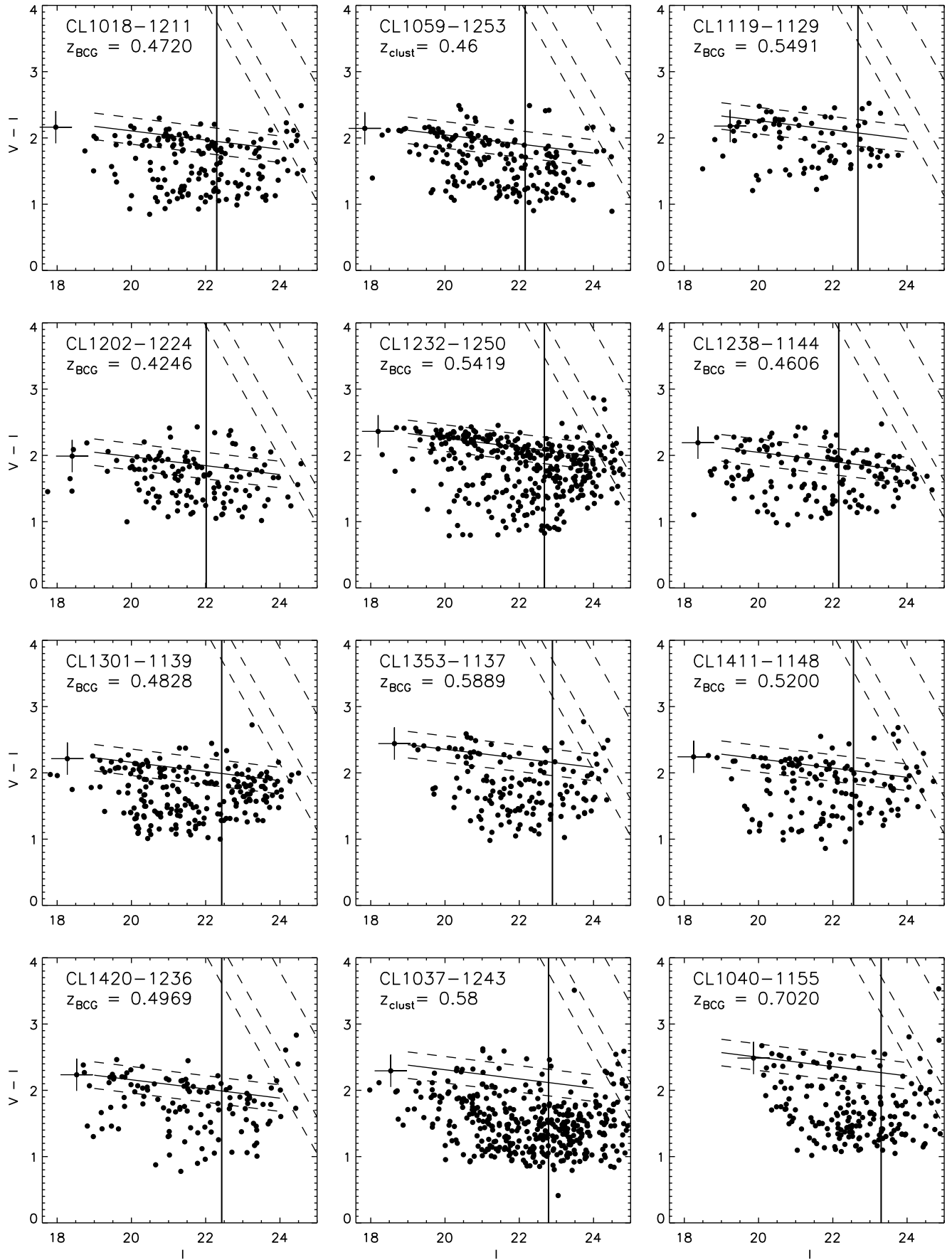


Figure 5.

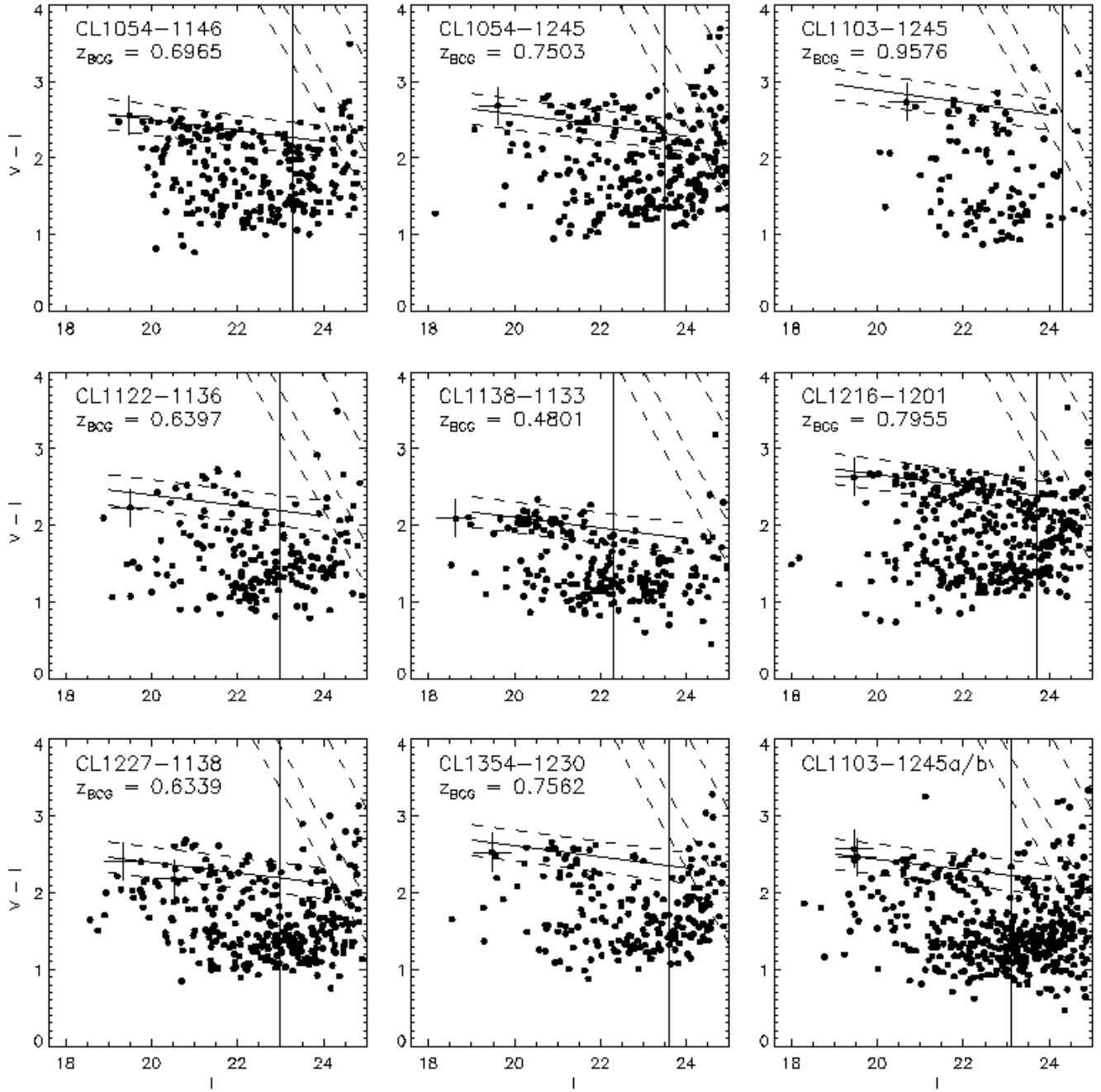


Figure 5. –continued. $V - I$ versus I colour-magnitude diagrams for galaxies projected within 1.0 Mpc of the BCG candidate (except for cl1227.9–1138, see text) in each of our 20 EDisCS fields. Galaxies for which our photometric redshift routines give a low probability of being near the cluster redshift have been eliminated. The BCG candidate itself is shown with a large cross. (Note that for cl1227.9–1138 the BCG candidate is outside our 1 Mpc circle.) The expected position of the red sequence is shown by a solid line, while a band within ± 0.2 magnitudes of this sequence is delineated by dashed lines. We use the count of galaxies within this band and brighter than the vertical solid line to estimate the richness of each cluster. Steeply slanting dashed lines show 1, 3 and 5σ detection limits for our V-band photometry. The final panel shows a colour-magnitude plot for the two additional structures away from the LCDCS detection in the field cl1103.7–1245. Filled circles represent here all the galaxies within the largest square field for which we have both IR and optical data.

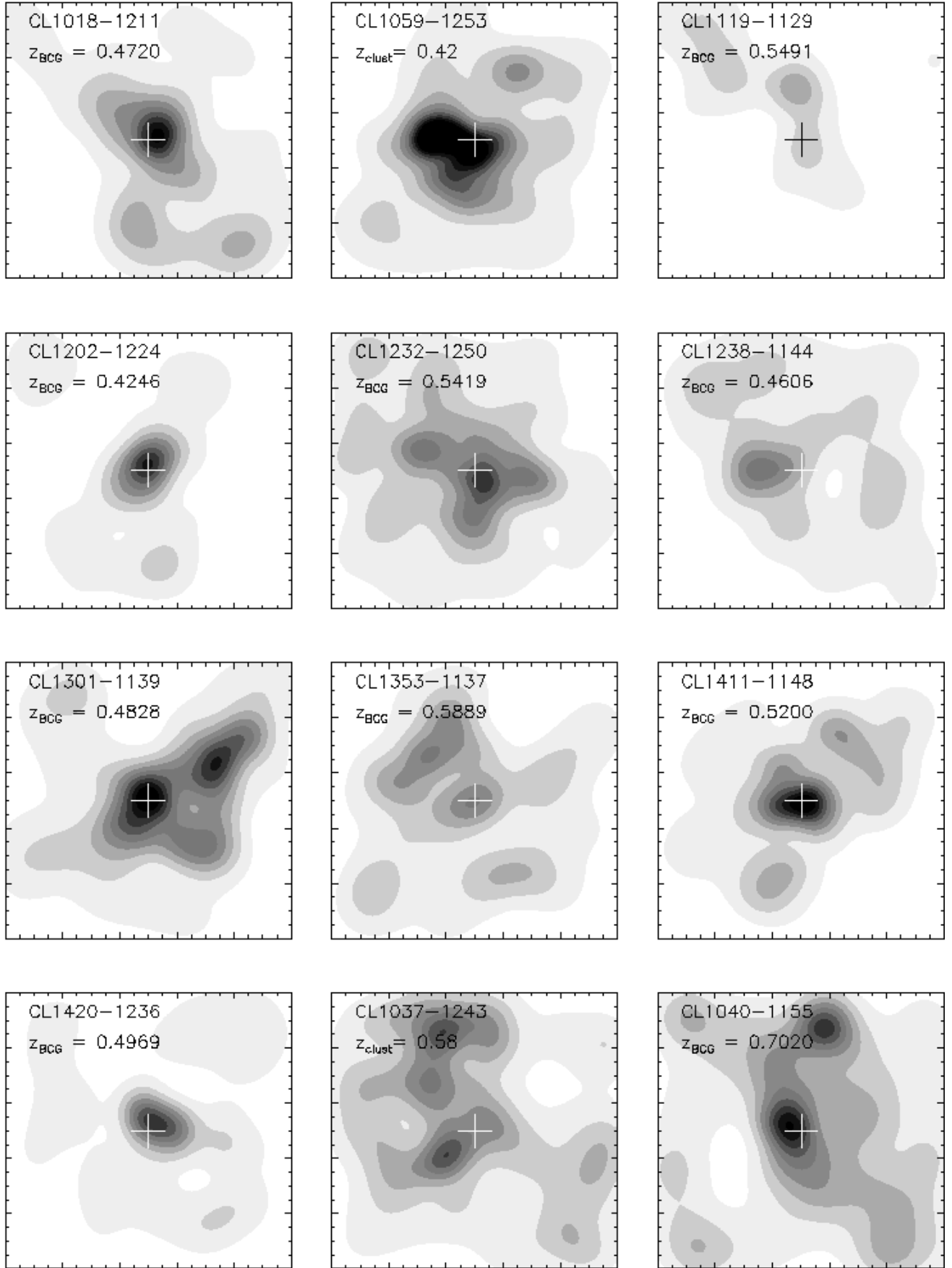


Figure 6.

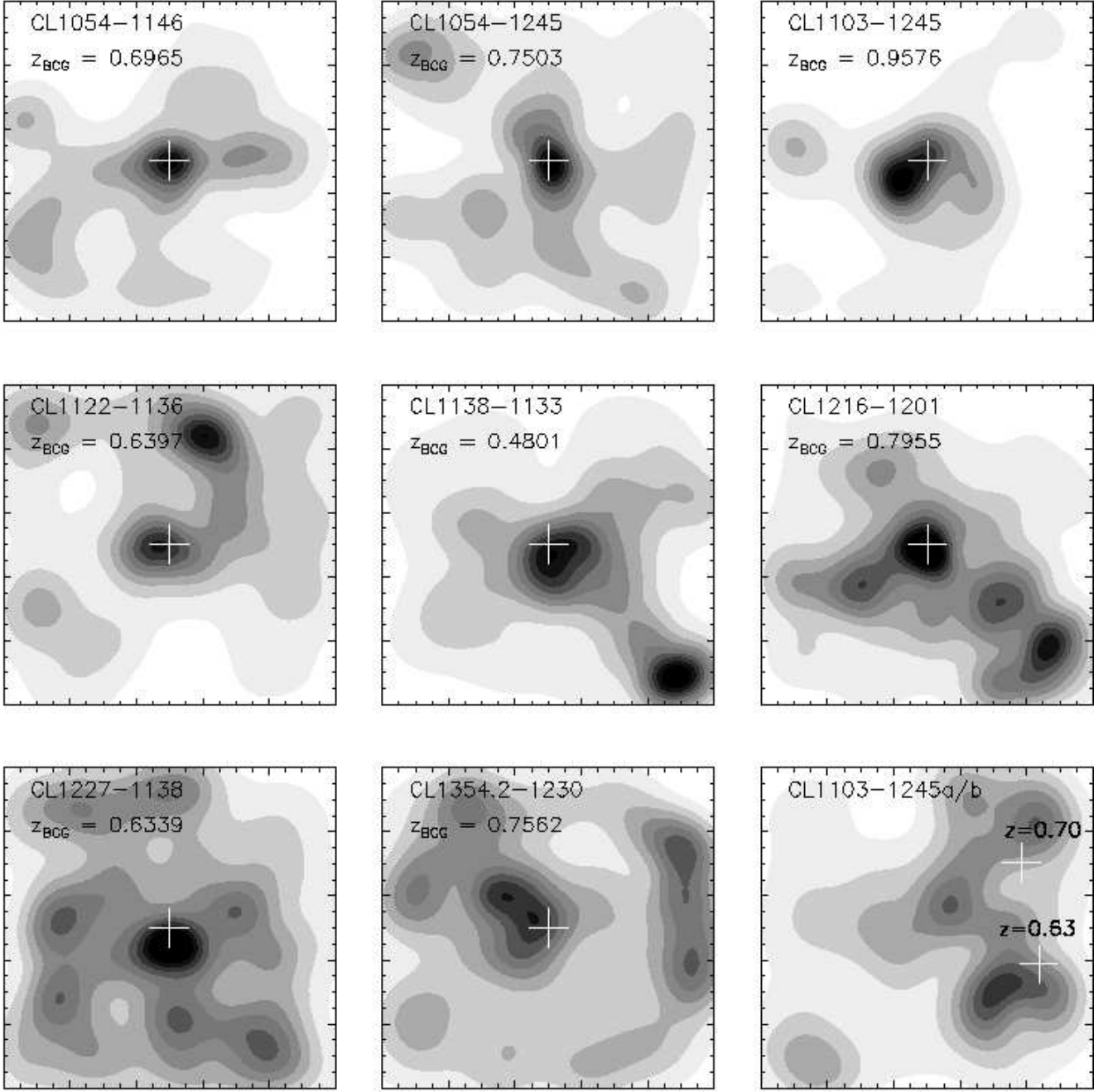


Figure 6. – continued. Adaptively smoothed isopleths for the surface density of galaxies brighter than $I = 25$ for a $4'8 \times 4'8$ EDisCS region centred on the BCG candidate (except for cl1227.9-1138, see text) in each of our fields. Stars and galaxies with photometric redshifts inconsistent with being close to the cluster redshift are eliminated before contouring. The lowest contour level plotted corresponds to 7.2 galaxies per square arcminute. Subsequent contours correspond to further steps of 7.2 galaxies per square arcminute for clusters cl1232.5-1250, cl1037.9-1243, cl1054.4-1146, cl1054.7-1245 and cl1216.8-1201. In all other cases subsequent contours correspond to steps of half this size. The position of our BCG candidate is noted in each plot by a cross. As in Fig. 1, north is at the top and east at the left of each map. The final panel shows isopleths for the two additional structures away from the LCDSCS detection in the field cl1103.7-1245.